Università degli Studi di Padova

Department of Information Engineering

Master Thesis in Electronic Engineering

Laser Reflectometry for Temperature Estimation of short-circuited IGBT Modules

Supervisor
Prof. Matteo Meneghini
Università degli Studi di Padova

Master Candidate
Paola Jakuza

Co-supervisor
Prof. Francesco Iannuzzo
Aalborg University

Student ID
2020185

Academic Year
2021-2022
Date
05 October 2022

Abstract

The project focuses on the use of the laser reflectometry technique, usually employed for studying thin films, in an innovative way: conduct thermoreflectance measurements to determine directly the junction temperature of an IGBT module short-circuited. The thermoreflectance measurement, a non-destructive and non-contact technique, consists in employing a laser beam and measuring the reflected light, whose amplitude changes as the temperature of the DUT. Therefore, it is possible to relate the measured light with the temperature. The junction temperature is a key parameter to study the reliability of an IGBT module under thermal stresses during operation.

Contents

Chapter 1

Introduction

Pulsed Photothermal reflectance (PPR) technique has been largely used to study the band structure of semiconductors and the thermal properties of novel thin film materials. Kading *et al.* were the first to use PRR in 1994 to measure the thermal conductivity of SiO_2 thin films [17]. Other applications include the study of thermal conductivity of TiAlSiN nanocomposite coatings with different Al/Ti atomic ratios [27]; the study of heat transfer of carbon nanotubes structures enhanced with Boron Nitride [16]; the measurement of interfacial thermal resistance between reduced graphene oxide (rGO) with its substrate [13].

The PPR experiment consist of a pump and probe setup. The sample is struck by a Nd:YAG (532 nm) laser pulse with a spot size (diameter of the laser beam) of the order of the millimiters, and a pulse energy of several millijoules. The probe laser consists of a 1 mW HeNe laser with a smaller spot size in the order of the micrometers and a wavelength of 632.8 nm, which is focused at the centre of the excitation spot. The pump beam monitors the sample's surface temperature that rises sharply and then relaxes with time thanks to the pump beam. The temperature excursion profile depends on the thermal properties of the surface. The surface temperature change of the sample induces a change in the refractive index n of the surface, that implies a change in the reflectance R. The reflectance variation ΔR is linearly dependant on the temperature ΔT through a temperature coefficient, called **thermoreflectance coefficient** c_{tr} which is material and light dependent and

must be derived through a calibration phase.

Recently, PRR has been used to study the temperature of integrated circuits (IC) as an "optical thermometer" [25]. The absolute temperature change of the chip surface is directly correlated to the reflectance measurements thanks to the calibration. In this case, the heat generation is provided by the joule effect while a short current pulse is applied to the circuit. Thus, the pump laser beam is not necessary. The current pulse has a width of $1\mu s$ and in general this ultra-fast technique detects reflectivity variations down to the picosecond regime [21].

The aim of this work is to apply the Pulsed Photothermal Reflectance technique in the field of power electronics to derive directly the junction temperature T_j of an Insulated Gate Bipolar Transistor (IGBT) module during short-circuit.

Nowadays, the current technology, that includes thermocouples, optical fibers and infrared cameras (IR), is not suitable to estimate the junction temperature in this regime due to the slow dynamic response, which falls in the millisecond domain, while a short-circuit measurement is in the order of the microseconds. In traditional measurements, the sample is treated through an invasive process that involve the decapsulation of the module, the removal of the top gel that isolates the chip from the environment and, in the IR measurements case, a black-paint that must be applied to increase the emissivity of the semiconductors. Instead, the PPR technology is suitable for ultra-fast, non-contact and non-desctructive measurements and it's a powerful tool that could help estimate a key parameter regarding the reliability of the IGBT module.

The high temperature that the module must sustain during short circuit induce thermal stresses that compromise the long-term reliability, and as a consequence the lifetime of the device doesn't respect the target one. Knowing the junction temperature can help estimate the stresses simultaneously at a semiconductor level and package level. This information is vital for applying a design-for-reliability approach in the design phase.

The thesis work is divided in the following chapters:

1. Chapter 2 - Reliability of short-circuited IGBT: The chapter will treat how the IGBT permeates in many different applications and why the

estimation of the junction temperature is important for a reliability point of view;

2. Chapter 3 - Theoretical background: explains qualitatevely the physics theory that is behind the dependance of the reflectance with temperature on the band structure level;

3. Chapter 4 - Experimental Setup: the experimental setup is described in detail

4. Chapter 5 - Experiment: presents the experiment methodology and results. It is divided in the following way:

   - Preliminary measurements, where the noise floor is evaluated;

   - Measurements with semiconductor sample, where initial measurements are conducted with a test sample instead of the IGBT device;

   - Calibration, done with different instrumentation and for both the test sample and the IGBT device;

   - Short-circuit measurement, that presents how the short-circuit will be conducted in a future measurements.

Chapter 2

Reliability of short-circuited IGBTs

2.1 Reliability in Power Electronics

From the 1960s, power electronics has gradually gained importance in a wide range of industries, from the automotive to the aereospace to the energy sector (photovoltaics PV and wind turbines), and it's expanding in applications for the distribution of electrical power, from the generation until the end-user site. Many efforts have been devoted to improving the performances of power electronic systems, especially in terms of power density and efficiency, through advancements in circuit topologies, control schemes, semiconductors and passive components technologies [31]. Recently, a shift in the research objectives have taken place towards the study of the **reliability** of power electronics. This is due to the needs of the different industries for more reliable power systems for safety constraints, on one side, and for more cost-effective and sustainable solutions on the other [31]. In figure 2.1 are illustrated the recent research trends in reliability-critical applications.

2.1.1 Field experience

From field experience, it emerges that power converters are the most fragile part in terms of failure rate, lifetime and maintenance cost. Examples are applications in wind turbines and PV installations.
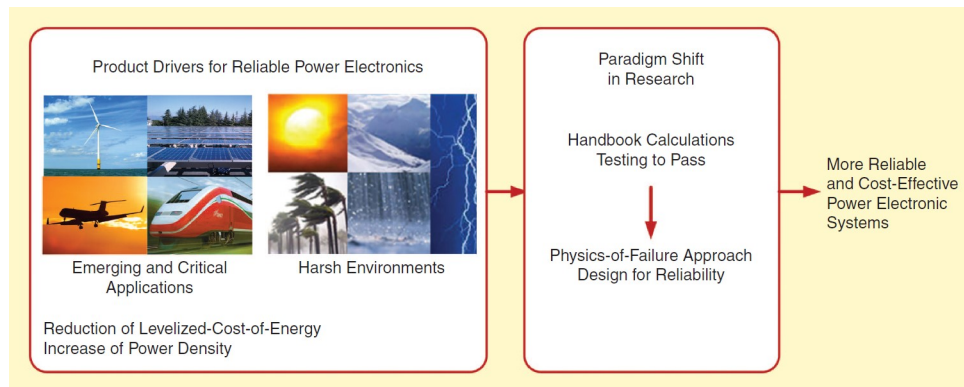
Figure 2.1: Research objectives shift. [31]

In wind turbines, power converters are employed to regulate the flactu-ating input power and to maximize the energy harvested from the wind [5]. In the report [26], the 35000 downtime events of 350 offshore wind turbines have been registered: it resulted that power electronic frequency converters cause the 13% of failures and 18.4% of downtime.

In PV applications, PV inverters are used to convert the harvested DC energy to the user AC grid or to integrate the output energy into the electrical grid [19]. Nowadays leading producers provide PV modules with a warranty of 20 years. However, PV inverters must be replaced up to 5 times during the lifetime of a PV module due to the fact that their warranty is of only 5 years. Thus, inverters produce additional investments throughout the lifetime of a module [31]. In the paper [22] a large utility-scale grid-connected photovoltaic (PV) system is under investigation for a period of 5 years (2001-2006). From the study, it emerges that inverters account for the 37% of unscheduled maintenance events and for the 59% of the related costs, as reported in figure 2.2.

As a conclusion, more reliable power electronics modules can prevent the failure of the overall system and reduce the maintenance costs of the main green energy producers. Thus, a comprehensive study of the reliability has significant implications in the sustainability and the world-wide electrical consumption.
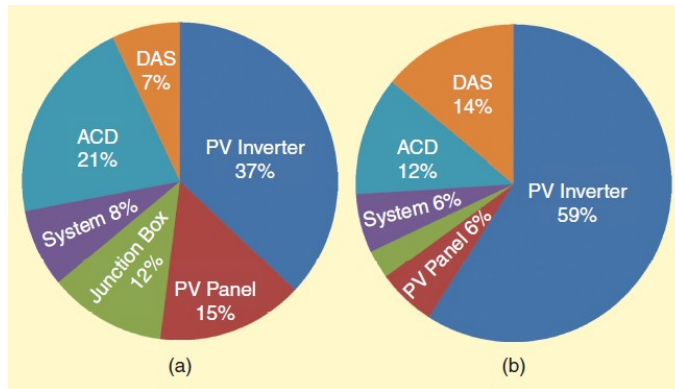
Figure 2.2: Field data of 3.5-MW PV plant [22]. (a) Unscheduled maintenance events by subsystem. (b) Unscheduled maintenance costs by subsystem.

2.1.2 Critical components in Power Electronics

At the component level, the most critical elements are the semiconductor switching devices (i.e. IGBTs, MOSFETs, PiN diodes, ecc.) and the capacitors. Two surveys were conducted to study the reliability-critical components in microelectronics and power electronics systems [32, 33]. The first survey confirms that the semiconductor devices and the capacitors are the most vulnerable components, which mainly fail due to temperature, vibrations and humidity, as reported in the second survey. Steady-state **temperature** and power cycling are the main stressors that lead to failure, as illustrated in figure 2.3.
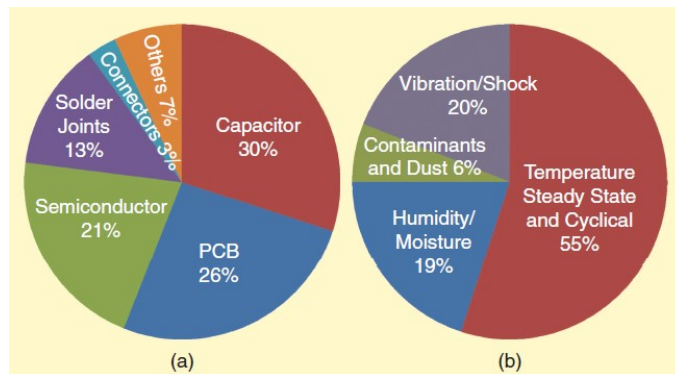

Figure 2.3: Surveys on failures in power electronic systems. (a) Failure distribution among major components [32]. (b) Source of stress distribution for failures [33].

This thesis focuses on the study of the **Insulated Gate Bipolar Transistor**

(IGBT), since it is the main power device employed in many high-profile industries, as reported in figure 2.4, due to its many advantages, such as good power handling capabilities, high speed switching capability, relatively simple voltage controlled gate driver, short-circuit robustness, etc. [8].
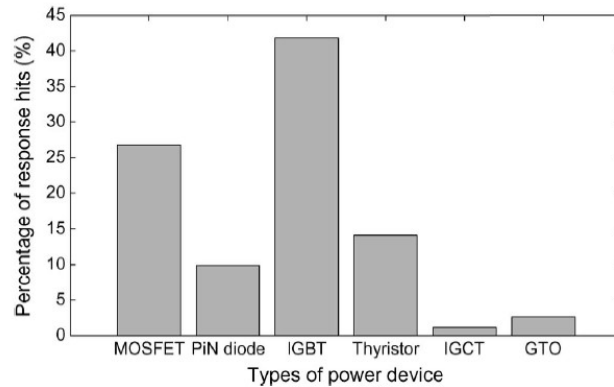

Figure 2.4: Survey on the type of power devices employed in high-profile industries [33].

2.2   Structure of an IGBT module

The IGBT is a semiconductor device that combines the physics of the MOSFET with the bipolar transistor. The gate driver signal is applied to the power MOSFET structure. The output charateristic is instead typical of an BJT. Thanks to it high input impedance, the gate driver circuit is compact and low cost.

In practical applications, power devices are usually given in a package, called module, where many IGBT chips and Free-wheeling diodes (FWD) are packaged together. The package provides many advantages, such as possibility to create new power blocks designs, to provide electrical conduction from the IGBT and FWD to external circuitry, to transfer the heat generated by the chips to a heat sink [2]. A module presents a Direct Copper Bonded (DCB) substrate soldered to a base-plate. The DBC provides electrical isolation for the chips and a cooling system, together with the base-plate which is connected to a heat sink. The bond wires function is to connect the emitter to the substrate, which ultimately is connected to the external terminals. The
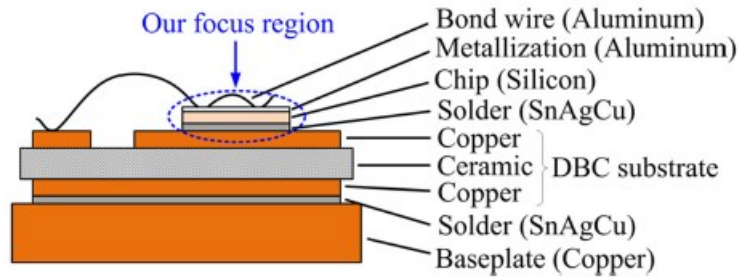
Figure 2.5: IGBT Module structure [3]

module is finally covered in silicon gel, or epoxy resin, for insulation.

Overall, the module is composed of several materials having different Coefficients of Thermal Expansion (CTEs), which are listed in table 2.1.

Material	$c_{TE}(10^{-6}/K)$
Al_2O_3	6.8
AlN	4.7
Si_3N_4	2.7
BeO	9
Al	23.5
Cu	17.5
Mo	5.1
Si	2.6
AlSiC	7.5

Table 2.1: Coefficients of thermal expansion CTE for different materials in al IGBT module

2.3 Failure Modes related to thermal stresses

During normal operation, the IGBT is used as a switch. As it turns ON and OFF, a pulsating heating flux goes through the chip causing active temperature cycling, called power cycling. The heat flux goes through all the layers of the module and since the module is made of materials with different thermal conductivities (CTE) and capacitances, a thermal gradient is
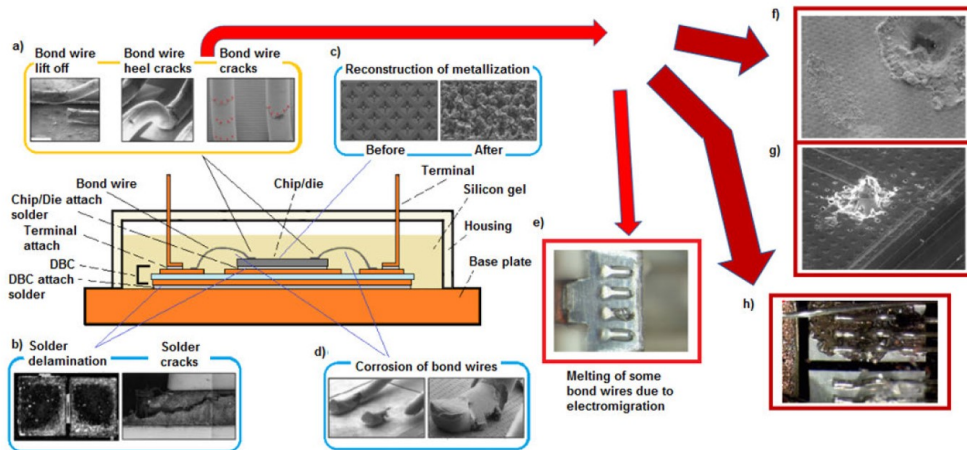
Figure 2.6: IGBT Module degradation and related failures under thermal failures [2]

caused. Repetitive expansion and contraction of the layers with different CTE finally induces thermo-mechanical stresses on each interface between different materials. The region of interest of the module in this treatment is the **metallization** on top of the Si chip, where bond wires are connected. The metallization is made of Aluminum, therefore the Al/Si interface is under investigation. Thermal stresses are responsible for long-term reliability issues.

Some of the degradation effects include bond-wire degradation, solder degradation, metallization degradation, stress corrosion of bond wires, melting due to electro-migration, localized melting of the metallization near the bond wire pds due to current crowding, localized melting of metallization due to hot spots formation, metling of metallization due to over temperature [2]. Those effects can be seen in figure 2.6. The most common failures are bond-wire ageing and solder fatigue, which are coupled mechanisms since one degradation mechanism accelerate the other and vice versa. A solder degradation causes the local temperature increase, that accelerates the bond wire lift-off.

IGBTs operate under harsh conditions at a high junction temperature and can undergo **random failure** events, such as overcurrent, overvoltage or short-circuits. Short-circuit events can occur due to other components fail-

ure or unwanted turn-on of the switches caused by strong electro-magnetic interference [7]. Random thermal and mechanical stresses compromise the reliability of the component since they are a source of a large uncertainty in the lifetime estimation. Thus, predicting the current, strain and temperature distributions are vital for a design-for-reliability approach. [3]. In order to correctly estimate the lifetime of a device, not only normal operation must be considered, but also abnormal events such as short-circuits.

2.4 Junction Temperature estimation

As mentioned above, the power devices are the most-reliability critical part in a power electronics system and the main stressors are the temperature swing and the steady-state temperature, whose effect on the device are extensively studied through power cycling. However, also short-circuit events must be investigated since the IGBT can undergo short circuit operation in many applications.

Estimating the junction temperature is vital from the reliability point of view as it helps estimating some degradation effect, such as oxide degradation at the semiconductor level, die attach and bond wire degradation at the package level [7].

Nowadays, the technologies available cannot measure directly the junction temperature in this regime. Traditional technologies, like thermocouples, thermistors and optical fibers, are able to detect variations in the order of the millisecond, which is not enough accurate in the short-circuit measurement. Ultra-fast infrared camera are able to acquire variations down to $1\mu s$, but due to the low emissivity [1] of light of silicon, it is not possible to accurately correlate the emitted light of the sample with its temperature. In order to mitigate this effect, the device is treated by decapsulating, removing of the gel and black-painting the surface .

Another technique is lock-in thermography, where the infrared camera measurement is combined with a lock-in measurement approach. However,

---

[1]It is possible to correlate the temperature of a body from its irradiance thanks to the Stefan's blackbody radiation law, where the area of the irradiance is directly proportionae to the fourth power of the temperature through Stefans constant

IR camera measurement are intrinsically invasive on the device under test and is not suitable for some applications.

An indirect technique has aso being developed: TSEP or Temperature-Sensitive Electrical Parameter [7], where a electrical parameter temperature-dependent can be easily monitored and then correlated to the temperature change. In [7] the short-circuit collector current of an IGBT device is monitored and the junction temperature is derived thorough the use of a map, that linearly correlates T_j with V_{CE} and I_{SC}.

Chapter 3

Theoretical Background

The electrical and optical properties of materials depend on their band structure, such as on the dispersion relation, that correlate the energy $E(\mathbf{k})$ with the wavevector $\mathbf{k}$. In the following, the band structure of aluminum will be investigated qualitatively in order to justify how the reflectivity varies with temperature as mentioned in chapter 3. Firstly, the absorption coefficient will be described in general; then it will be analyzed in the particular case of Aluminum. Finally, the energy gap variation with temperature will be correlated to the temperature-dependence of reflectivity and other optical properties of aluminum.

3.1   Absorption Coefficient

A photon can be effectively absorbed exciting an electron in the higher energy level if the levels respect the k-selection rule, where the momentum is maintained constant and only vertical transition are possible (see fig. 3.1a). This limited pairs of states are called joint density of states $\rho_j(\nu)$ for the energetic transition $E = E_2 - E_1 = h\nu$, which is given by [1]

$$\rho_j(E = h\nu) = \frac{1}{2\pi^2}\left(\frac{2m_r^*}{\hbar^2}\right)^{3/2}\sqrt{E - E_G} \qquad (3.1)$$

---

[1]General result for Silicon. See [18]

where m_r^* is the reduced mass of the electron; E_G the energy gap of the material.

The absorption coefficient $\alpha(\hbar\omega)$, that expresses how much light can penetrate in a material before being absorbed, strongly depends on the band structure of the material since a photon can be absorbed if it has an energy equal to or higher than the energy gap E_G. The absorption coefficient depends on the momentum matrix element and on the joint density of states and can be described by the following equation ([2])

$$\alpha(\hbar\omega) = C_0 |\hat{e} p_{cv}|^2 \frac{1}{2\pi^2} \left(\frac{2m_r^*}{\hbar^2}\right)^{3/2} \sqrt{\hbar\omega - E_G} \qquad (3.2)$$

where $|\hat{e} p_{cv}|^2$ is the momentum matrix element calculated from the Bloch functions of electrons in the valence and conduction bands; m_r^* is the reduced mass of the electron; $\hbar$ the reduce Planck's constant. From eq. 3.2 it can be observed that the absorption coefficient is $\propto \sqrt{\hbar\omega - E_G}$ with the cutoff energy $E = E_G$ below which no absorption is possible (see fig. 3.1b). Thus, the absorption coefficient depends on the wavelength of light and on the material considered. In figure 3.2 it can be seen how the $\alpha(\lambda)$ strongly depends on the material considered since each material presents an unique band structure.

3.2 Optical Absorption in Aluminum

3.2.1 Aluminum band structure

It the literature it has been proved that also metals present a band structure that govern their optical properties. This was done by studying the absorption of electromagnetic energy at microwave and far infrared ranges [4]. Particular points in the joint density of states called *critical points* are responsible for their optical response [20].

In the particular case of Aluminum, it has been proved that its band structure is almost free-electron like, presenting degenerate **parallel bands**. Due to this

---

[2]General result for Silicon. See [18]
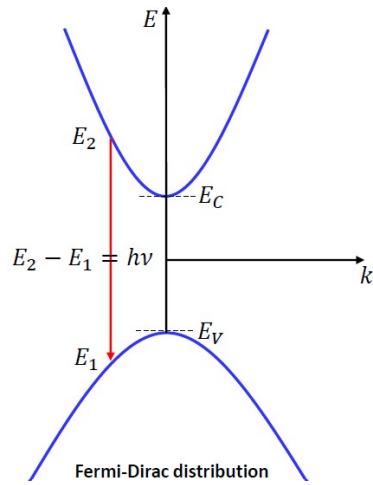
(a) Representation of the k-selection rule in the energy-momentum 1D plot with parabolic bands approximation
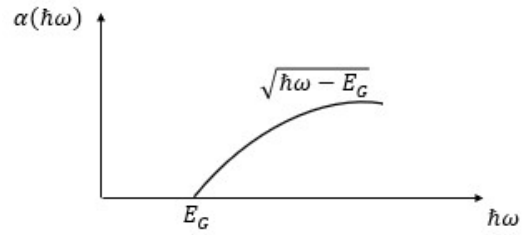
(b) Qualitative plot of the absorption coefficient vs. energy

structure, the critical points of Aluminum lie, with the highest probability, in simmetry points [10]. Thus, the main optical properties of Aluminum are determined by the interband transitions of electrons within critical points.

In figure 3.3c it is considered the section of [110] plane of the Brillouin zone, where it is possible to observe how the bands split due to a small crystal potential V. In [10] a study has been done to provide the energetic transitions responsible for the peak present at around $E_{peak} \approx 1.6$ eV in both the complex dielectric constant $\epsilon_2(w)$ and absorption coefficient $\alpha(\omega)$ of Aluminun. The peaks are illustrated in figures 3.4.

The calculated band structure of Aluminum reported in fig. 3.5 is employed to observe that the only transitions at symmetry points are

$$W_{2'} \longrightarrow W_1$$
$$\Sigma_1 \longrightarrow \Sigma_3 \qquad \qquad (3.3)$$
$$W_3 \longrightarrow W_1$$

The first two transitions have a gap energy of 1.4 eV, while the third one of 2 eV respectively. In general, the region around W contribute to the main peak. The peak then falls to zero due to the predominance of the free-electron behaviour. Other transitions that contribute to the peak are those in the proximity of the [110] axis at the Σ zone since the second band above the

Fermi level and the third band below are **parallel**. The transitions energies of $W_{2'} - W_1$ and $\Sigma_1 - \Sigma_3$ agree within an uncertainity of 0.1 eV with the peak of $\epsilon_2(\omega)$, while the transition energy of $W_3 - W_1$ is 0.6 eV larger. In conclusion, the main inter-band transitions that produce the peak in the optical constants of Aluminum are those around the regions W and Σ of the Brillouin zone.

3.2.2   Aluminum Energy band gap dependence with T

The energy band gap of Aluminum is temperature-dependent. The relation between band gap and temperature has been derived experimentally in [4] by extending the previous study on the absorption of electromagnetic energy to lower temperature and smaller wavelengths. In the study it was also derived the band gap at $T = 0°K$, $E_G(0)$. The general result is a **decrease** of the band gap as the temperature of the sample increases. This happens because as T increases the position of the bands shift due to temperature-dependent lattice dilation and temperature-induced transitions of electrons, different from the normal absorption transitions. In figure 3.6 it is possible to observe the fitted experimental data. In addition, a comparison with the theoretical curve predicted by the BCS (Bardeen-Cooper-Schrieffer) theory is present. [3]

3.2.3   Optical constants dependence with T

The effect of the energy gap decrease on the frequency-dependent optical constants is the rigid shift towards lower energies of the functions. Thus, a **red shift** is present and influences all the waveforms of the optical constants. In the present experiment, the reference energy of the laser source is 1.96 eV since

$$E_{laser}[eV] = \frac{1240}{633\,\text{nm}} = 1.96\,\text{eV} \tag{3.4}$$

As the temperature increases, the red shift causes the optical constants to whether increase or decrease with respect to the reference laser energy, depending on the waveforms. In the case of Aluminum, the peak in the absorp-

---

[3]The study includes the superconductivity feature of Al. Superconductivity is the property of a material of having zero electrical resistance below a certain temperature, called critical temperature T_C

tion is positioned at $\lambda_{peak} = 775$ nm, thus at a higher value than the reference of the laser. In this case, the red shift implies a decrease in the optical constants of Aluminum, as reported in figure 3.7, where the refractive index and the extinction coefficient are plotted. A comparison with Silicon is present to appreciate how different materials behave as their T increase. In this case, n and k increase, opposed to the Aluminum case.

The reflectance R of a material can be derived by the following relation (see [28]):

$$R = \frac{(n-1)^2 + k^2}{(n+1)^2 + k^2} \tag{3.5}$$

It can be noticed that an increase(decrease) in n and k imply an increase(decrease) in R. Consequently, the expected behavior of reflectance with temperature in the Aluminum case is a **decrease** of reflectivity as the temperature **increases**. In chapter 5, this relation will be experimentally demonstrated.

3.3 Thermoreflectance technique

The considerations done above can be summarized in the following equation

$$\frac{\Delta R}{R} = \frac{1}{R}\frac{dR}{dT}\Delta T = c_{tr}\Delta T \tag{3.6}$$

where c_{tr} is the thermoreflectance coefficient that **linearly** correlates the reflectance variation with the temperature. c_{tr} depends on the material under investigation and the wavelength of the light source. Usually, it is in the order of $10^{-2} - 10^{-5}K^{-1}$ [29] and it must be determined for each device under test. By the use of a photodetector, it is possible to directly correlate the difference in relative reflectivity with the variation of the **detected voltage**, since

$$\boxed{\frac{\Delta R}{R} = \frac{\Delta V}{V} = c_{tr}\Delta T} \tag{3.7}$$

The thermoreflectance coefficient is only known for some bulk materials at certain wavelengths and under certain experimental conditions. Therefore, it must be determined each time the DUT and the experimental setup change through a preliminary calibration phase. Once the coefficient is known, it is

possible to normalize the measured voltage signal to obtain the temperature profile. Thus, this technique enables to derive a direct evolution of the temperature of the DUT.

A requirement for the device surface is to be coated with a metal thin film, preferably Aluminum or Gold, for the purpose of enhancing heat absorption and capturing the surface temperature [12].

3.4   Conclusions

In this chapter it has been justified how the reflectivity should vary with temperature. This was done by analyzing qualitatively the material properties, in particular the band structure and the relation of the optical constants with energy. Moreover, the optical constants were related to the energy of interest, the laser energy. In this way, it is possible to predict and verify during the experiments if the setup correctly detects the predicted relation presented in section 3.3.
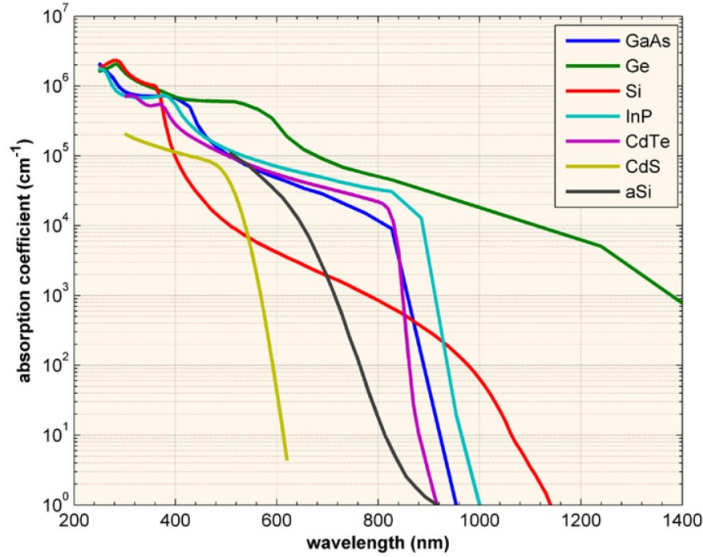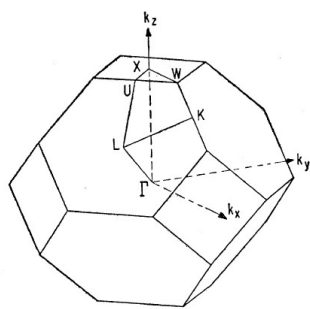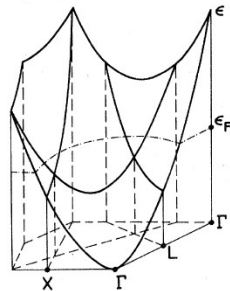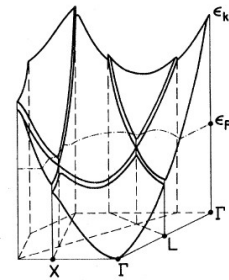
Figure 3.2: Absorption coefficient in different semiconductor materials at 300K. See [6]

(a) Brillouin zone for a cubic lattice. See [14]

(b) Section of (110) plane of the Brillouin zone in Al electron-free. See [23]

(c) Splitting of degenerate bands when a small crystal potential is present. See [23]

Figure 3.3: Brillouin zone of Aluminum

(a) Absorption coefficient due to parallel bands. See [23]

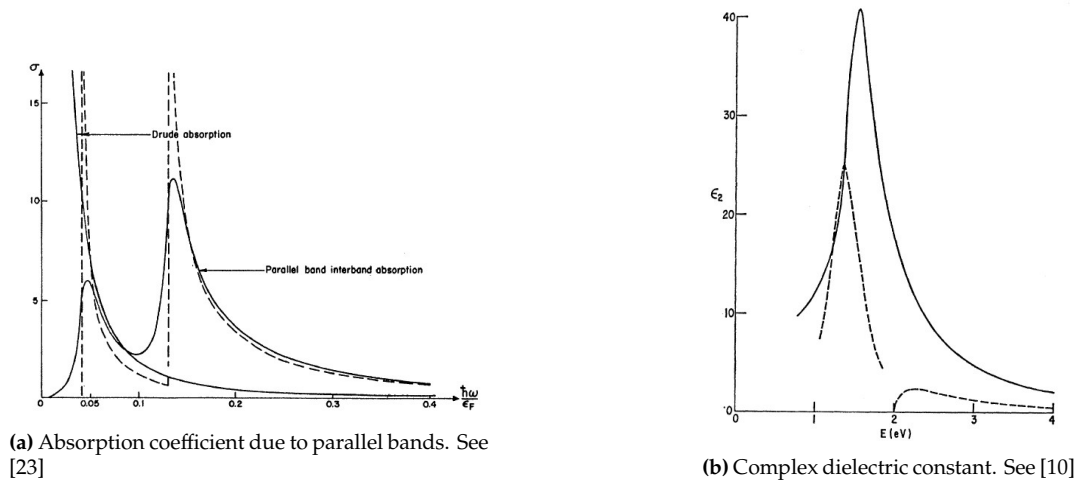(b) Complex dielectric constant. See [10]

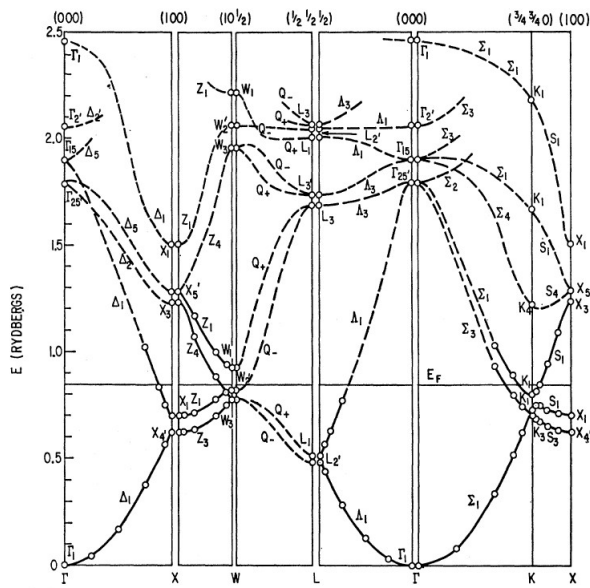**Figure 3.4:** Peaks in the optical constants of Aluminum due to inter-band transitions

Figure 3.5: Band structure of Aluminum along simmetry axis. Circles represent calculated points. See [10]
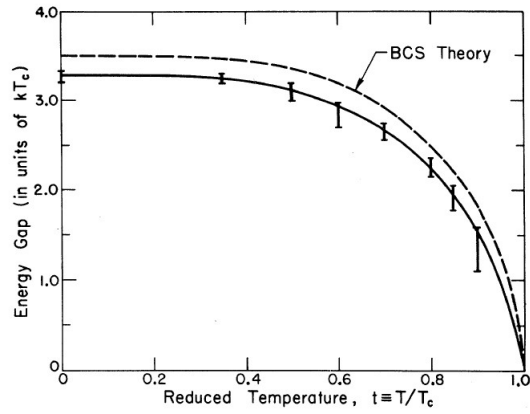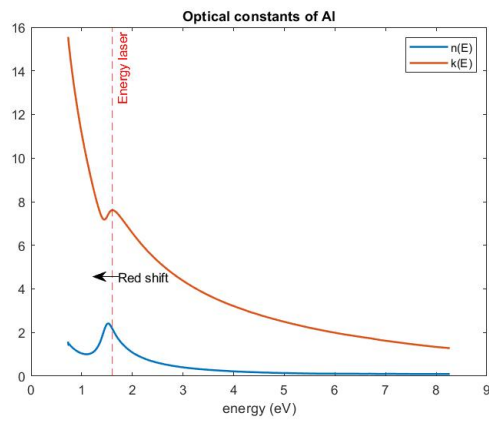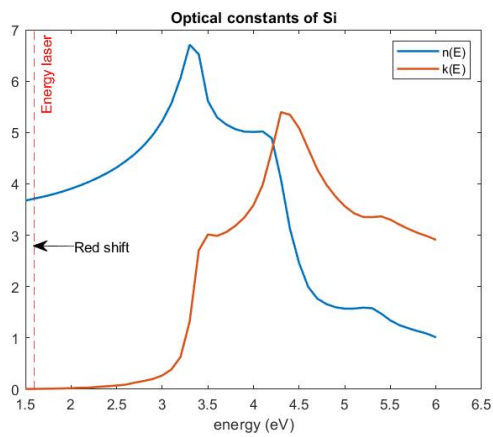
Figure 3.6: Energy band gap relation of Aluminum with Temperature. See [4]

(a) Refractive index and extinction coefficient of Aluminum. Data from [24]

(b) Refractive index and extinction coefficient of Si. Data from [24]

Figure 3.7: Comparison optical constants. (a) n and k of Al (b) n and k of Si

Chapter 4

Experimental Setup

4.1 Overview

The devices employed in the setup are the following (fig. 4.1):

- Continous Wave (CW) HeNe laser HRS015B (fig. 4.1a) with:

  - $\lambda = 632.98\,\text{nm}$
  - Output Power $> 1.2\,\text{mW}$
  - Beam diamater $0.65 \pm 0.05\,\text{mm}$

- Si photodetector PDA8A2 (fig. 4.1b)

- USB 2.0 CMOS Camera (fig. 4.1c)

The devices are mounted on an cage system (fig. 4.2) composed by several optical components:

- Motorized stage

- Polarizing Cube Beam Splitter (PBS)

- Nd Filter

- Non-polarizing Cube Beam Splitter (NPBS)

- Two 45° angle mirrors
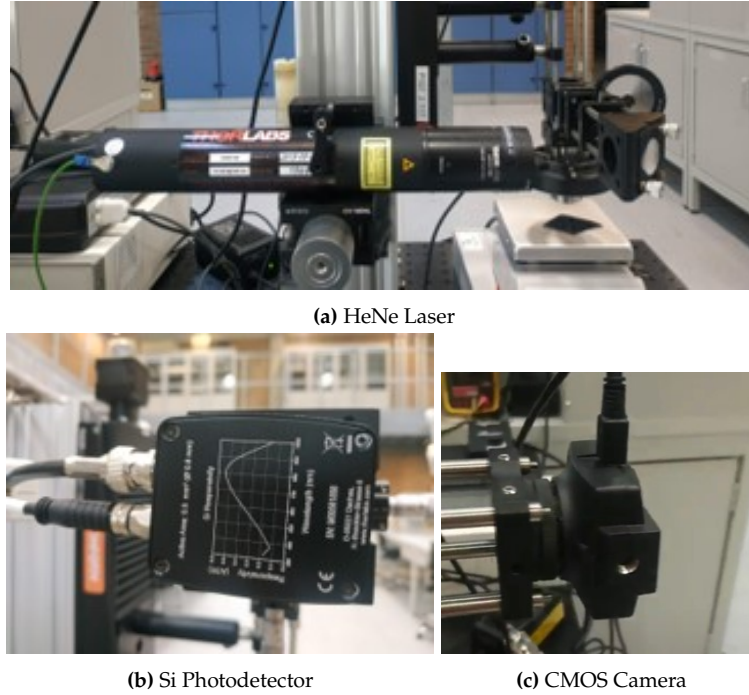
- 5X Microscope Objective MY5X-802

(a) HeNe Laser

(b) Si Photodetector   (c) CMOS Camera

Figure 4.1: Devices employed in the setup

Laser Operation   The continous-wave HeNe laser presents two different operation modes: frequency stabilization and intensity stabilization modes, where a feedback system controls a heater that expands or contracts the laser tube changing the cavity length and thus the modes allowed to oscillate (see Appendix B.2 for details). In this experiment, the laser is used in intensity stabilization mode.

Microscope   The microscope focuses the beam spot on the DUT. Since the numerical aperture of the microscope is $NA = 0.14$, the spot size d on the DUT can be derived from the following equation:

$$d = 1.27 \frac{\lambda}{NA} = 1.27 \times \frac{0.633}{0.14} \mu m = 5.742 \mu m \tag{4.1}$$

The microscope presents a working distance of $34mm$, thus the device must be positioned at this distance for a correct focusing.

Light Path

The output light of the laser is coupled into the cage system by a 45° angle mirror, mounted on a two adjuster kinetic mount. The light passes through a lens and a Nd filter, which can be set in order to reduce the optical power of the beam or it can be left inaltered. The beam goes through a polarizing cube beam splitter (PBS) and it directly hits the sample. The sample surface is positioned at 90° with respect to the impinging light, thus the reflected light is perpendicular to the surface. The beam is focused by a microscope (MO) positioned at the end of the cage system to prevent light scattering. A LED illuminator is present and it can be turned on to visualize better the beam. The reflected light from the surface's sample passes through the PBS and hits a second 90/10 non-polarized beam splitter (NPBS), which transmits 90% of the light and reflects the 10%. The reflected light hits the CMOS camera, whereas the transmitted light is deflected by a second 45° mirror into a lens and photodetector. In figure 4.3 is showed a schematic of the setup.

4.1.1   Optical Alignment and Operation

Laser Turn On

To turn on the laser the key must be rotated. It takes up to 15 minutes for the output light to stabilize. In section 5.1.2 the data from the stabilization phase can be found. The laser is mounted on a z-y mount and can be adjusted so that the beam is aligned inside the cage system.

Detector operation

The output of the photodetector can be connected to a multimeter to check the alignment of the beam. Initially, the voltage on the multimeter reads a value in the order of the mV. To achieve a correct alignment a value between 1V-3V must be read. The ND filter is removed for the initial alignment.

DUT positioning

The DUT must be placed at 90° with respect to the beam so the reflected light has the same direction of the impinging one. A bullseyes is used in order to level the kinematic platform surface, where the DUT is placed. The knobs are rotated until the bubble is placed in the centre.

Beam Focusing

The optics is mounted on a z motorized stage that permits to move the setup up or down with high precision.
Firstly, the beam must be focused on the DUT. This means positioning the DUT at the microscope focal length of 34 mm, which is achieved by moving the setup on the z axis. The focusing is correct when the maximum voltage is read from the photodetector.

Alignment

Once the beam is focused, it is adjusted so that in each point of the cage system the beam is positioned in the centre. This is assessed by the use of a cage plate. The first 45° angel mirrors are adjusted so that light enters in the middle of the PBS. The second mirror is positioned to make the light hit the centre of the Si chip on the photodetector. It is also possible to adjust the position of the detector, which is placed on a x-y mount. The operation is done by monitoring the multimeter to get the maximum voltage. Once the alignment is satisfactory, the Nd filter is repositioned so to decrease the output power of the light in order to not saturate the photodetector. Finally, in figure 4.5 the light path can be seen once the setup is correctly aligned.
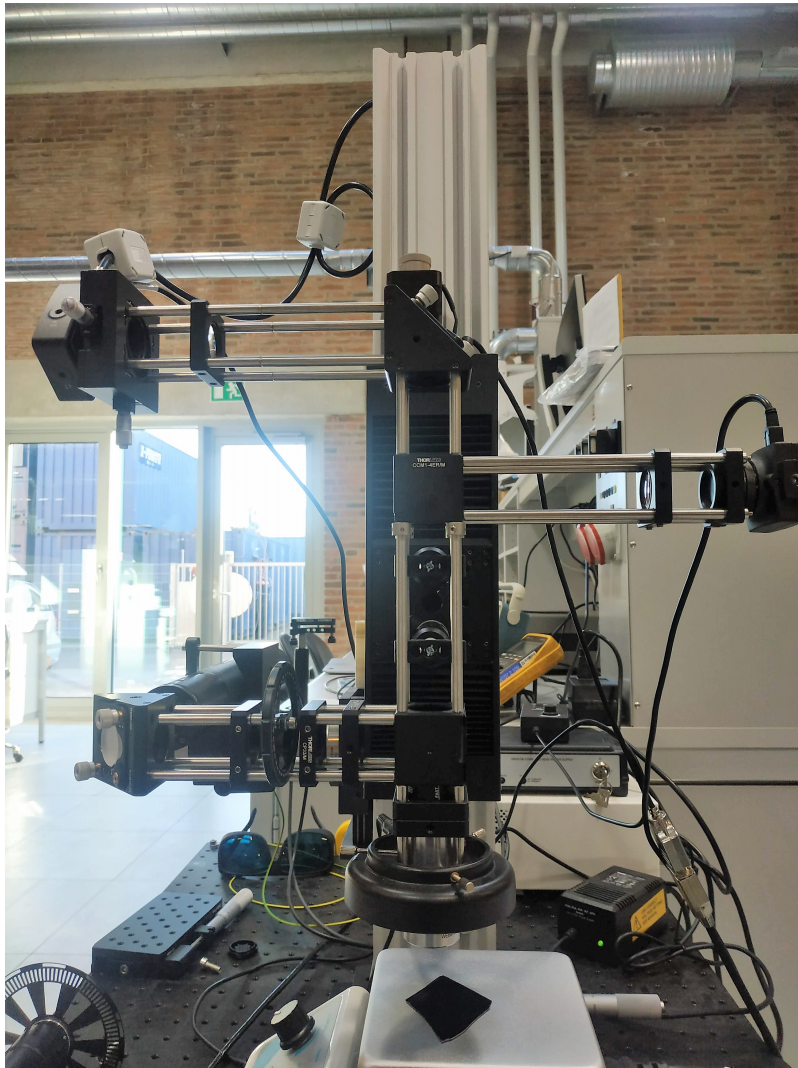
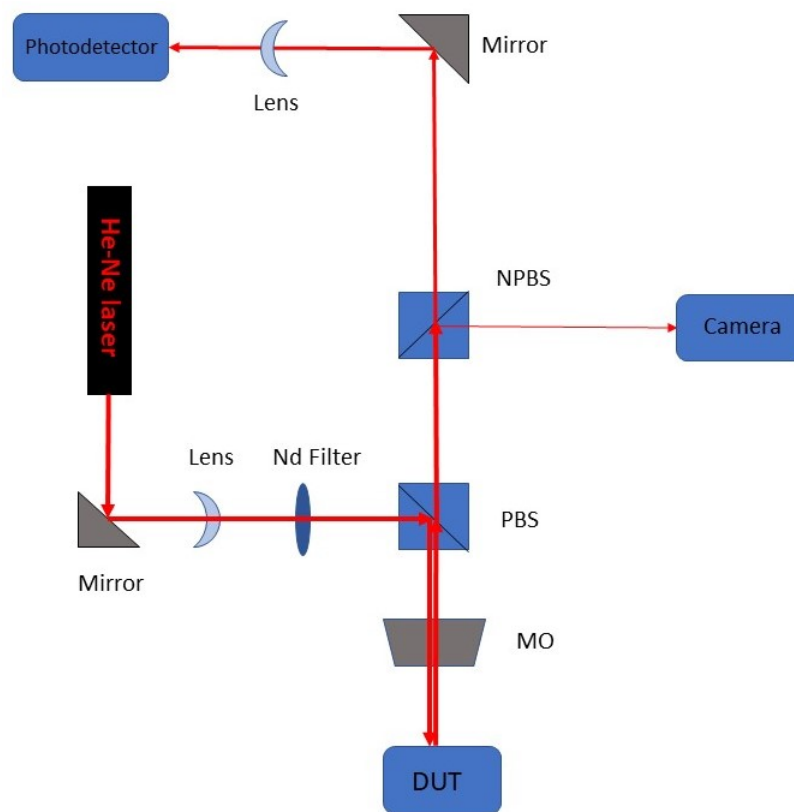**Figure 4.2:** Experimental Setup: optical components and devices
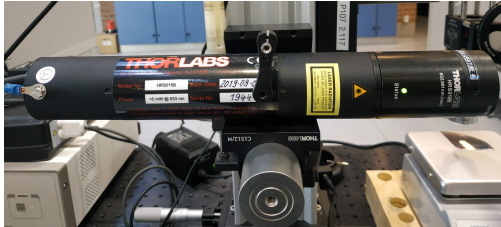
Figure 4.3: Experimental scheme

(a) HeNe Laser head

(b) Laser Power Supply

(c) Multimeter
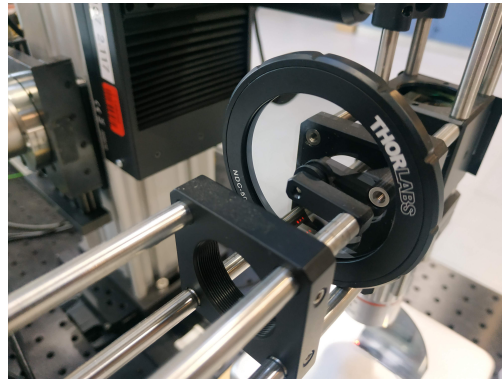
(d) Nd Filter

(e) Z knob
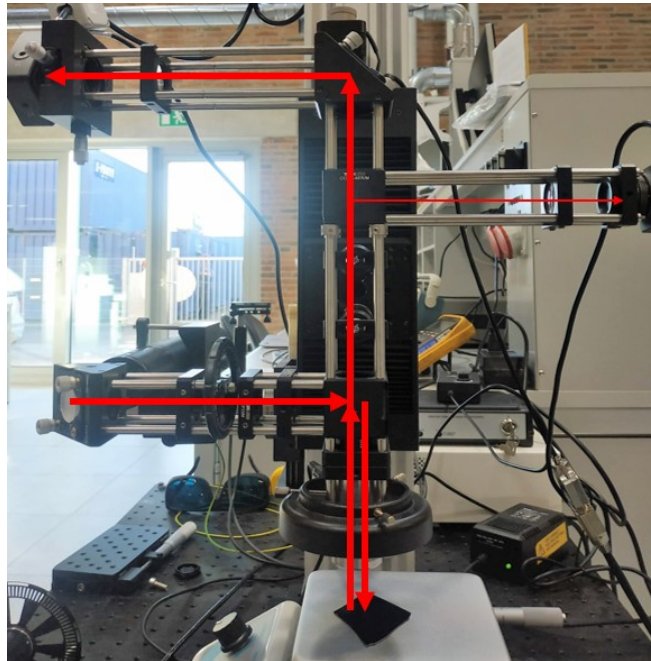
Figure 4.4: Elements of the setup

Figure 4.5: Light Path

Chapter 5

Experiment

5.1 Preliminay measurements

The aim of the preliminary measurements is to assess the noise floor and the offset inherently present in the setup and that will determine the uncertainty of the future measurements. The following analysis focuses on the electrical noise of the photodetector, the optical noise of the laser and a countermeasure to reduce the noise. Additional results on the initial warm up of the laser are included.

5.1.1 Noise Floor Evaluation

Photodetector Noise

Initial measurements highlight the presence of a noise floor and an offset due to the photodetector. A dark measurement shows a dark offset amplitude, which is $-2.36\,\text{mV}$, as reported in fig. 5.1a), in agreement with the reported datasheet value, comprised between $\pm 10\,\text{mV}$ (see table 5.1). It is observed that the negative amplitude of the dark offset is in part compensated by the room light (see fig. 5.1b), that increases the negative offset to $-1.22\,\text{mV}$.

	Amplitude [mV]	Peak-to-Peak [mV]
Dark Offset	-2.36	2.00
Ambient Offset	-1.22	20.4
Laser	-	24

Table 5.1: Noise Measured Data

Laser Noise

The laser output is very stable: from the datasheet the fluctuations are the 0.03% with respect to the optical output power, as can be seen in the data in fig. 5.1c and 5.1d. The laser noise is mainly coming from the drifting of the lasing cavity lines in and out of the gain curve and it is composed of frequency components from less than $1Hz$ to several Hz.

The noise was measured both in DC coupling and AC coupling. In the latter, the low frequency fluctuations are attenuated due to the high pass filter of the AC coupling, which cuts out the frequency components below $10Hz$ (see fig. 5.1e). Therefore, the noise was measured in DC coupling by changing the offset of the oscilloscope to get a better resolution (see fig. 5.1f). However, as the reflected laser light from the sample is measured, a much higher fluctuations of around $30\,mV$ pk-pk is measured from the photodetector, as reported in table 5.1. It is concluded that the noise is not optical but electrical and it must come from the measuring device, thus the photodetector.
As the photodetector is switched on, the noise floor increases, thus it is hypothesized that the noise derives from the $\pm12V$ DC power supply of the sensor.

Noise Reduction

An attempt to lower the noise was to substitute the sensor's power supply with the lab DC power. However, an improvement was not obtained (see fig 5.2), thus the floor noise considered for the setup is of around $30\,mV$ pk-pk.
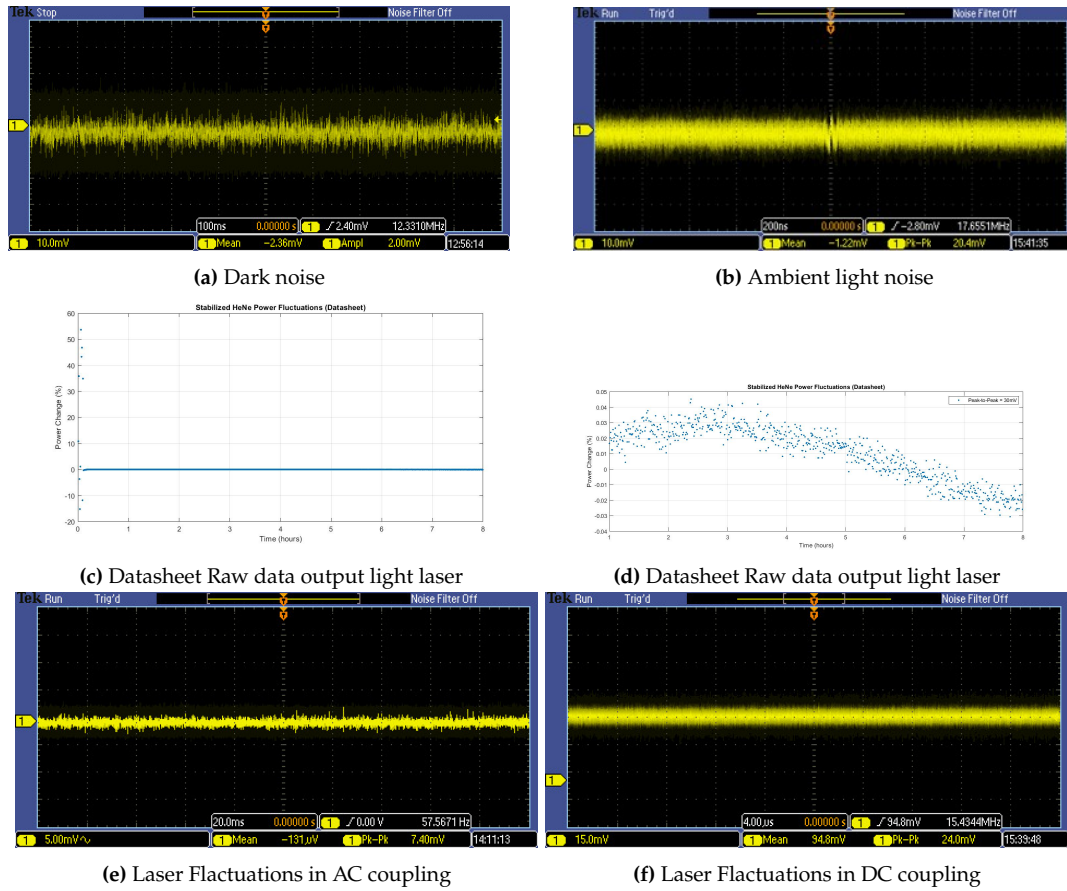
(a) Dark noise

(b) Ambient light noise

(c) Datasheet Raw data output light laser

(d) Datasheet Raw data output light laser

(e) Laser Flactuations in AC coupling

(f) Laser Flactuations in DC coupling

Figure 5.1: Devices Noise Evaluation

(a) Photodetector Ambient noise before replacing the power supply

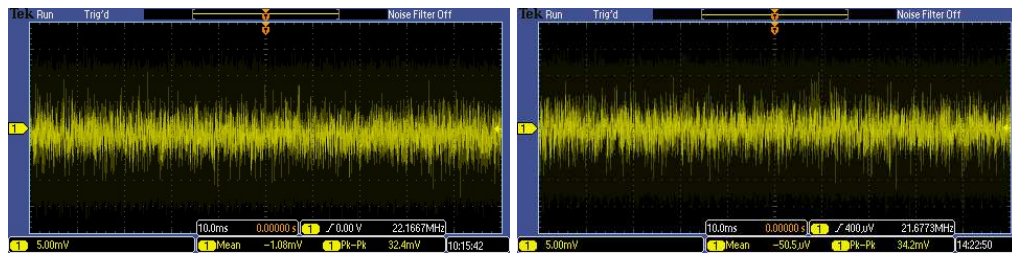**(b)** Photodetector Ambient noise after replacing the power supply

Figure 5.2: Photodetector noise comparison - before and after changing power supply

5.1.2   Laser Stabilization

The laser can be operated in two different modes: frequency or intensity stabilization, where whether the frequency or the output optical power of the light is kept constant through a feedback system where the length of the cavity is adjusted. In this experiment the laser is operated in intensity stabilization mode. As the laser is turned on, it takes up to 15 minutes to stabilize.

In fig. 5.3b it is possible to observe the detected light of the photodetector as the output light of the laser stabilizes. The initial oscillation has a frequency of 2 Hz, since its period spans to 5 divisions with a scale of 100 mV per division. After the laser is warmed up it can be used to conduct the experiment.

5.2   Measurements with semiconductor sample

The aim of the initial measurements is to asses the relation described by equation (3.6) by testing a simple piece of semiconductor since it is more immediate to predict and verify the relation. A piece of silicon with an Aluminum coating was tested. The metallization is employed in reflectance measurements to improve the reflectivity of the surface.

In this phase the setup is slightly modified: a heater replaces the kinematic platform thus the DUT is positioned on the heater itself during the measurements. In this way it is possible to monitor the voltage change as the sample is heated up. In figure 5.4 is shown the preliminary phase setup.
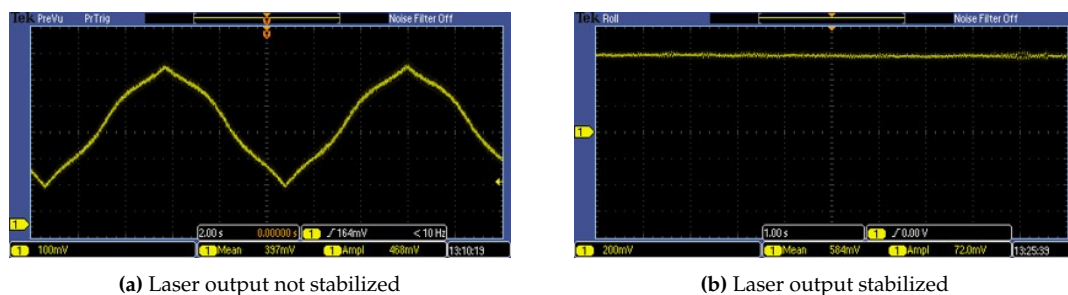

(a) Laser output not stabilized   (b) Laser output stabilized
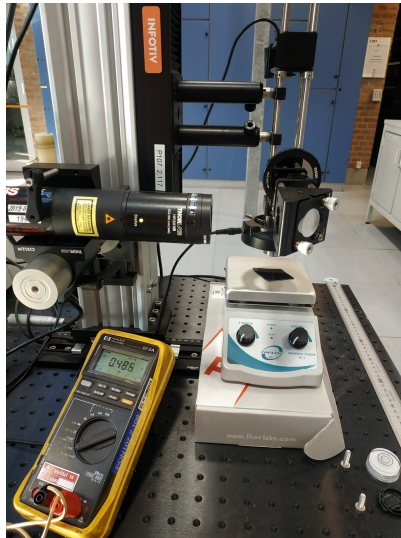
Figure 5.3: Laser stabilization

Figure 5.4: Preliminary tests setup

5.2.1   Silicon sample with Aluminum coating

Initial measurements attest the validity of the relation described by the equation 3.6. From figure A.1 it is possible to observe some photoreflectance measurements, where the signal varies with the temperature of the sample as it is heated and cooled down. The heater is able to go up to 300 °C, thus to appreciate the change in the reflected light, the knob is turned to the maximum value.

In most of the experiments it is observed a decrease of the reflected light in the heating phase and an increase in the cooling one. However, in the first measurement it is observed an inverse relation. Since it was an exception, the measurement was neglected. In order to better understand how the beam varies when the sample is heated, the CCD camera was used to visualize the beam spot on the sample. It is observed a drift of the beam spot on the sample as it heats up (see fig. A.2).

5.3   Calibration - Silicon Sample

The calibration goal is to determine the thermoreflectance coefficient of the device under investigation c_{tr}, that depends on the material of the DUT and

the wavelength of the source. This is done by heating the device and recording both the change in the reflected voltage and the relative temperature in order to make a map of the T versus V. Ultimately, it will be possible to correlate the photothermal signal with the surface temperature by scaling the signal by c_{tr} [25]:

$$\Delta T = c_{tr}^{-1} \frac{\Delta R}{R_0} \qquad (5.1)$$

5.3.1 Calibration with Infrared Camera (IR)

Setup Initially, an infrared camera was used to measure the temperature of the sample. In particular, the camera FLIR E40 was used, depicted in figure 5.6. The camera was mounted on a tripoid in order to make the measurements repeatable. The sample was adhered to the heater with a silicon thermal paste in order to achieve the same temperature between sample and heater. The measurement was done by heating the sample and saving several points $(T(t_i); V(t_i))$, where $T(t_i)$ is the temperature measured from the IR camera, and $V(t_i)$ the voltage measured with the oscilloscope, both taken at the same instant t_i. This was done both during the heating and cooling phase. Approximately 10 points were saved for each phase from 25 °C to 80 °C distant 5 °C each. The heating lasted approximately 20 minutes, instead the cooling 45 minutes.

Initial measurements with the IR camera highlighted the issue of low emissivity of the semiconductor sample. From figure 5.5 it is possible to observe that if the IR camera was pointed on the sample, the measured temperature was much lower (47 °C) than the actual one, corresponding to the temperature of the heater (249 °C).

Thus, the IR camera was pointed to the heater plate instead of the sample to get a realistic temperature.

Measurements results The measurement of the voltage and the temperature were taken simoultaneously on the IR camera and the oscilloscope. Afterwards, the points were associated by referring to the same time instant. With this procedure, the experiment was repeated and four maps were ob-

Calibration phase	$c_{tr}(V/°C)$
1	-1.821×10^{-2}
2	-1.625×10^{-2}
3	-1.579×10^{-2}
4	-1.729×10^{-2}

Table 5.2: Thermoreflectance coefficients - slope of the heating phase of the maps

tained, as depicted in figure 5.7. The error bars indicate the uncertainty on the voltage measurement, give by the peak-to-peak value of the measurement. The uncertainty on the temperature measurement is not available from the IR camera.

A comparison between the heating phases was done and a linear regression fit was applied to the maps. In table 5.2 are listed the slopes of the maps, which correspond to the thermoreflectance coefficient. It can be seen that the coefficient is negative, as expected for Aluminum, and that the order of magnitude is in the order of 10^{-2}.

Considerations

1. Non matching of the heating and cooling phases, while they should be identical if the same physical process is investigated

2. If a certain reflected voltage is considered, i.e. 1.95 V, the corresponding temperature of the sample in the cooling phase is 40.7 °C instead in the heating phase is 30°C.

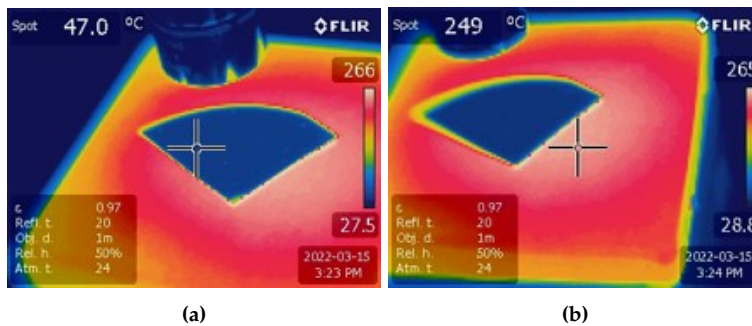(a)   (b)

Figure 5.5: Initial measurements with the IR camera. (a) IR pointed on the sample. (b) IR pointed at the heater plate

This suggests the presence of a thermal capacity of the sample that slows the heat flux as the sample dissipates heat during the cooling phase. A **delay** of the heat dissipation between sample and heater can result in registering a heater temperature which is lower than the actual one of the sample.

3. The cooling phase is shifted upwards with respect to the heating phase, while the expected behaviour should be opposite.

   The hypothesis is that the reflected voltage measurement is correct, instead the temperature can be not accurate since the heater temperature is measured.

   A delay in the dissipation of the heat between the sample and the heater implies that the measured heater temperature is actually lower than the one of the sample.

   The delay is supposed to be present only in the cooling phase, thus the temperature registered in the heating phase is approximately equal to the sample temperature.

   Looking at the cooling phase, if a certain temperature is considered, i. e. 35.5°C, this corresponds to the heater temperature. The reflected voltage is 2.03V.
   However, 2.03V corresponds to a temperature of 25°C in the heating phase, that is supposed to be the actual temperature of the sample.

$$T_{heater,cooling} = 35.5°C$$
$$T_{sample,cooling} = 25°C$$
(5.2)

   This means that 35.5°C is the heater temperature, while 25°C the sample's one during the cooling phase, which is in contradiction with what is expected since the sample should have a higher temperature that takes a certain amount of time to dissipate.

   Thus, the curve should be shifted downwards (see fig 5.8).

4. From previous considerations, what is measured is the temperature of the heater and not the one of the sample itself. There could be a delay

also between the heating of the heater and of the sample.

5. An optical fiber can be used in substitution of the IR camera in order to get the exact temperature of the sample during the experiment.

5.3.2   Calibration with fiber optics

Setup   Due to the considerations in the section 5.3.1, an optical fiber was then used to measure the temperature of the sample and carry the calibration measurements. The optical fiber provides real-time measurement and was placed approximately 1 cm from the laser point. Both heating and cooling were measured. Several points were registered distant approximately 5°C each. The heating phase lasted approx. 10 min and the cooling approx. 1 hour.

Measurement procedure   In this case, the optical fiber allows to record the temperature real-time with an accuracy in the order of the ms. Thus, the data from the fiber optics provide a time vs temperature graph during the entirety of the heating/cooling. The voltage instead can be saved at certain time instants t_i on the oscilloscope. The procedure carried to compose the map was to associated the voltage reflected from the sample to its temperature thanks to the time indication present on the oscilloscope and the data from the fiber optics. Beforehand, the oscilloscope and the fiber optics software times were synchronized. In figure 5.10 is depicted how the data were elaborated.

Measurement results   In figure 5.11 are depicted the maps that resulted from the data analysis, where an **hysteresis** is present.

In this measurement it is possible to get a temperature uncertainty. The time accuracy of the voltage measure is in the order of the seconds, while the one of the temperature is in the order of the milliseconds. Thus, within a second it was possible to attach to a selected temperature its variation, as represented in figure 5.12. When the variation was not monotonically increasing or decreasing, as in fig. 5.12a, the highest and lower temperature within the interval were considered as upper and lower bounds and the

Calibration phase	$c_{tr}(V/°C)$
Heating	-1.262×10^{-2}
Cooling	-1.139×10^{-2}

Table 5.3: Thermoreflectance coefficients - slope of the heating and cooling phase of the first calibration maps

average was the point reported on the map. In figure 5.12b is represented the first calibration with the temperature uncertainty for some selected points. It can be observed that the temperature uncertainty can be neglected with respect to the voltage uncertainty.

A linear regression fit was applied to the points in calibration n. 1 to derive the slope and thus the c_{tr} coefficient (fig. 5.12d). In table 5.3 are reported the results of the applied fit for both the heating and cooling phase. As in the measurement with the IR camera, the coefficients are negative and in the order of 10^{-2}.

Considerations

1. The voltage in calibration 1 spans from 1.34V down to 48.2 mV, thus reducing considerably. Therefore, the laser beam intensity should reduce as well until it is barely visible. However, the laser beam is always visible throughout the heating and cooling. This suggests that the beam is beeing deflected out of the photodetector by the heater plate movements during heating.

2. Another indicator is the presence of the hysteresis, that indicates geometrical modification of the heater plate due to thermal dilatation.

3. A third factor was the order of magnitude of the c_{tr}. From [9], it was found that the c_{tr} of pure aluminum is $-4.02 \times 10^{-5}/°C$, in contrast with the values found experimentally, in the order of 10^{-2}.

4. It was concluded that the reflectivity change wasn't correctly measured with this setup mainly due to the geometrical movements of the heater plate that moved the sample surface. As a consequence, the beam is

being deflected out of the active area of the photodetector. From initial measurements in Appendix A.2, it emerged that the laser spot was deflected during the measurement. This is an unwanted behaviour since only the intensity of the beam should vary as the reflectance varies.

Ultimately, the heat generation was substituted.

5. In the next measurements, the silicon piece was replaced with the IGBT device. In this way, it is possible to heat the chip directly by applying a DC bias, without the use of an external heater that can disturb the measurements.

5.4   Calibration - IGBT Device

5.4.1   First experiment

Setup   The device employed is a novel IGBT module FP50R12KT4 (fig. 5.13a), which is previously decapsulated in order to remove the gel. The IGBT was mounted on the holder in order to prevent any movement, with a heat-insulating paper positioned under the device to limit the heat dissipation. The device was fixed to the holder to ensure the stability of the laser spot on the chip. The heat generation was provided by DC biasing the device thanks to a DC power supply, connected such as CH 2 provided the input (V_G, I_G) and CH 1 the output (V_{CE}, I_C) (figure 5.13b). For the optical alignment, the laser beam is centered on the Aluminum metallization of the chip, where bond wires are connected. The optical fiber was positioned on the same chip to record the temperature (figure 5.13c), which is mounted on an optical fiber holder (figure 5.13d).

Optical Alignment   During the optical alignment, additional disturbances are observed. Initially, the disturbances are due to an incorrect optical alignment where unwanted reflections from the bond wires are detected. Once the alignment is adjusted, greater low frequency flactuations are observed with an amplitude of approximately $60 \, \text{mV}$, whereas in the silicon sample

trace had an amplitude of approximately $40\,mV$. A complete analysis of the noise is done in section 5.4.2.

Measurement procedure   The procedure for the calibration is the same adopted for the silicon sample: the temperature profile over time is available from fiber optics; from the oscilloscope some instants were saved in which the reflected voltage was changing. Then, the temperature and voltage are associated at a certain time instant t_i. The heating through DC biasing took approximately one hour, as the cooling and the temperature range considered is $T = [25; 75]°C$.

Measurement Results   The resulting T versus V maps in figure 5.15 show consistency between the heating and cooling phase, however a significant noise is present in the measurement. A linear regression fit is applied to the points and an increasing curve is observed, while from the theory in chapter 4 it should be decreasing for aluminum. One of the indicator of the goodness of the fit, R^2, is low for all the maps showing that the thermoreflectance change is not properly measured since it is buried in noise. In addition, the thermoreflectance coefficient derived continue to have an order of magnitude too high for the typical value for pure aluminum (see table A.1).

5.4.2   Second experiment

Noise Analysis   In the following analysis, the type of noise is analyzed in order to better understand what causes it.
Both the channel and the photodetector noise, presented in section 5.1.1, are thermal noises and they are intrinsic of the measurement devices. This noise has high frequency components that can be easily filtered with the low-pass filter of the oscilloscope.
As the laser is turned on, fluctuations at low frequency appear, with frequencies that range from $f_{low} = [10; 388.592]Hz$. Thus the trace presents low frequency oscillations with a superimposed thermal noise (see figure 5.16). The latter is filtered with the low-pass filter of the oscilloscope, with a cut-off frequency of $f_C = 6kHz$. As a consequence, the amplitude of the signal

decreases from $130mV$ to $80mV$. The lowest cutoff frequency is desired since the signal of interest is DC. Thus, with the filter ON the contribution to the noise is only given by the low frequency fluctuations, that cause high error bars in the calibration maps (see figure 5.16).

Due to the regularity of this fluctuations, it was hypothesized that the cause are electromagnetic waves frequencies that are picked up by detector coming from multiple sources. The wavelengths of this fluctuations are calculated as

$$\lambda = \frac{c}{f} \tag{5.3}$$

with c speed of light and they range from $\lambda = [772; 30000]km$. This interval falls within the radio wave wavelengths, mainly within the **SLF** (Super Low Frequency) band, that covers the range from 1000 to 10000 kilometers. This range includes the frequency for AC power grids (50 hertz and 60 hertz) [1], which could be the possible sources of noise.

The noise is accentuated also by environmental factors, such as people talking, walking, working with electronic equipment, causing floor vibrations that disturb the stability of the optical table.

In conclusion, both high frequency and low frequency components are present. The high frequency noise can be filtered out with the low-pass filter, whereas the low frequencies must be removed in a different manner. Environmental factors contribute to vibrations of the setup that resulted in vibrations of the sample and the laser head.

Lock-in amplifier   An effective way to reject the low frequencies is by means of a lock-in amplifier, which is composed by a homodyne detector followed by a low-pass filter. The lock-in amplifier is able to cancel the noise if the input signal is periodical. For this reason, an optical chopper must be used to alternate the optical light of the laser. The signal of the chopper, which is a square wave, will be used as a reference signal. If the frequency of the input signal is know and identical to the reference one, then all the frequencies different from the desired one are rejected, included the noise ones. The new setup is suitable for conducting optical measurements where the ΔR variation is very small in the order of $10^{-3} - 10^{-5}/°C$ where a signal-to-noise

ration is low, as mentioned in [30].

The additional required equipment is the following:

- External heater - two peltier cells

- Lock-in amplifier SR830

- Optical chopper with controller MC2000B

A schematic of the setup is depicted in figure 5.17.

Setup   The output of the photodetector is connected to the input A of the lock-in, while, the REF OUT signal of the chopper is used as external reference. The frequency selected for the chopper is f_{ref} = 100 Hz. The selected frequency must be such as the photodetector is able to sustain it. In this case, the photodetector bandwidth ranges from DC to $50MHz$ thus the reference signal is adequate.

Measurement procedure   In this case, the heat generation is produced by two peltier cells in order to control better the temperature. Since the peltier elements are current controlled, by regulating the current it is possible to set a desired temperature.

Once a desired temperature is reached after a transient (see fig. 5.18), the corresponding value on the lock in is saved. Then the points are plotted in a map.

Results   Two complete measurements were conducted. A linear regression was applied to the points. This time, what was expected emerged from the results.

Firstly, the curves are monotonically decreasing, thus the thermoreflectance coefficient is negative. Secondly, the order of magnitude of the coefficient is in the order of 10^{-4}, as predicted for aluminum in integrated circuits [11], where the effect of the passivation layer increases by one order of magnitude the coefficient with respect to the pure aluminum case. Moreover, the points are well fitted since the R^2 coefficient is high and both the curve are in agreement with one another.

Calibration phase	$c_{tr}(/^\circ C)$	R^2
Heating 1	-5.987×10^{-4}	0.9176
Heating 2	-6.81×10^{-4}	0.9786

Table 5.4: Thermoreflectance coefficients - slope of the heating and cooling phase of the three calibration maps

5.4.3 Conclusion

The lock-in was able to detect the small change in the thermoreflectance coefficient and to measure it correctly for the aluminum metallization in the IGBT module. The final value considered for the thermoreflectance coefficient is

$$\boxed{c_{tr} = -6.81 \times 10^{-4}/^\circ C} \tag{5.4}$$

since this estimated value presents the higher R^2 value. This coefficient will then be used to derive the junction temperature T_j of the device by simply normalizing the reflectance trace derived during short-circuit by c_{tr} (see relation 5.1).

5.5   Short-circuit Measurement

The short-circuit measurement is conducted on a PCB board designed within the Energy Technology department at Aalborg University for a power cycling test for Schneider Electric (fig. 5.20). The board is made of:

- IGBT module FP50R12KT4

- Six gate drivers 1ED020I12-F

- Four DC-DC converters for the power supply - Three MGJ2D121509SC and one NMJ1205SC

- Passive components - capacitances, resistors, diodes

The IGBT module is the same model as the one used in this work for the calibration. However, it has not been decapsulated so the gel is present.

Since the models are identical, the thermoreflectance coefficient, which is material dependent, is hypothesized to be the same for the two modules.

5.5.1   Desaturation signal

Since the board was not designed for a short-circuit measurement, some modifications must be made.

The gate drivers present a desaturation signal DESAT that blocks any short-circuit event since it is undesired during normal power cycling. Thus, in order to conduct the short-circuit measurement this signal must be bypassed. In a typical application, the output pin DESAT monitors the IGBT saturation voltage (V_{CE}) in order to detect desaturation caused by short circuits. If the IGBT is kept ON by the driver and the VCE is above a defined value and a certain blanking time has expired, the desaturation protection is activated and the IGBT is switched OFF (see [15]).

A diagram of a typical application for the driver is depicted in 5.22, where the desaturation signal is connected to the collector of the IGBT.

In the board, the desaturation is connected to a resistance Rdesat of $1K\Omega$ and a diode called Ddesat (see 5.21). The desaturation signal was thus disconnected from the collector of the IGBT by des-oldering the diode Ddesat and connecting what was the anode to the reference of the driver, or signal GND2. This was done by noticing that the anode of the zener diode ZDesat is connected to the reference of the driver,which is accessible from the back of the board, near to where the diode Ddesat was connected. By doing this, the signal DESAT is ultimately bypassed and the inverter can undergo short circuits.

5.5.2   Short-circuit Measurement

The additional laboratory setup required for conducting the measurement is the following (see fig. 5.23):

- PCB board for power cycling test on an IGBT module

- Pulse generator

- High voltage power supply - to provide the voltage supply for the IGBT module

The measurement is done by driving the gates of leg A of the inverter with a $10\mu s$ pulse with a $5V$ level. The short-circuit is obtained by driving both the drivers with the same signal, as depicted in figure 5.24.

During a short-circuit, the voltage across the IGBT is high and so is the current, which is 10 times higher than the nominal one. As a result high switching losses are present [3]. In figure 5.25a are depicted the typical current and voltage waveforms during a short-circuit.

It must be noted that the IGBT module is **non decapsulated** during the measurements, thus the laser beam is pointed on the IGBT chip with a coating of silicon gel. This technique is desirable since it is **non invasive** for the module, which does not need to be treated beforehand.

The expected measurement will be a photothermal signal of the light reflected from the surface of the IGBT that undergoes short-circuit. A sudden temperature increase is expected, thus the waveform will have a pulse-like shape, as depicted in picture 5.25b.

5.5.3 Results

The photothermal signal is characterized by a high noise, thus it is necessary to apply the average function of the oscilloscope to be able to observe the evolution of the optical light due to the short circuit. In figure 5.26a the following signals are represented:

- V_G Gate Voltage - provided by the pulse generator

- I_{SC} Short circuit current

- V_{CE} Output voltage

- V/V_0 Normalized Photothermal signal - with respect to DC value

In the first measurement it is possible to observe a **variation** in the optical response as a consequence of the thermal excursion of the chip during the

short circuit, proving that laser reflectometry is suitable for a short-circuit measurement.

In the second measurement the horizontal scale of the oscilloscope was increased in order to appreciate the complete evolution of the optical signal. In figure 5.26b it is possible to observe that by setting a horizontal scale in the order of the milliseconds, a **peak** in the optical response is present. The result is coherent with the expected photothermal signal (see 5.5.2).

These results prove that laser reflectometry is a technique that can be used effectively to observe the temperature evolution due to an event, which happens with a time interval in the order of the microseconds.

It is possible to increase the temperature of the chip during the short circuit by increasing the power supply. This is done in the third measurement in order to observe a higher optical peak. The supply voltage was increased from $V_{CC} = 250V$ to $V_{CC} = 280V$ (see figure 5.27a).

From the measured points it is possible to extract the value of the peak. In this case, the peak corresponds to

$$\frac{\Delta V}{V_0} = 8.43 \, \text{mV} \tag{5.5}$$

which can be converted in a temperature measurement, thanks to the thermoreflectance coefficient previously determined:

$$\Delta T = \frac{\Delta V}{V_0 \times c_{tr}} = 12.37°C \tag{5.6}$$

The quantitative value of the temperature peak does not correspond to a realistic value of the temperature excursion of an IGBT during short-circuit, however this can be an developed in a future work.

(a)

(b)

(c)

(d)
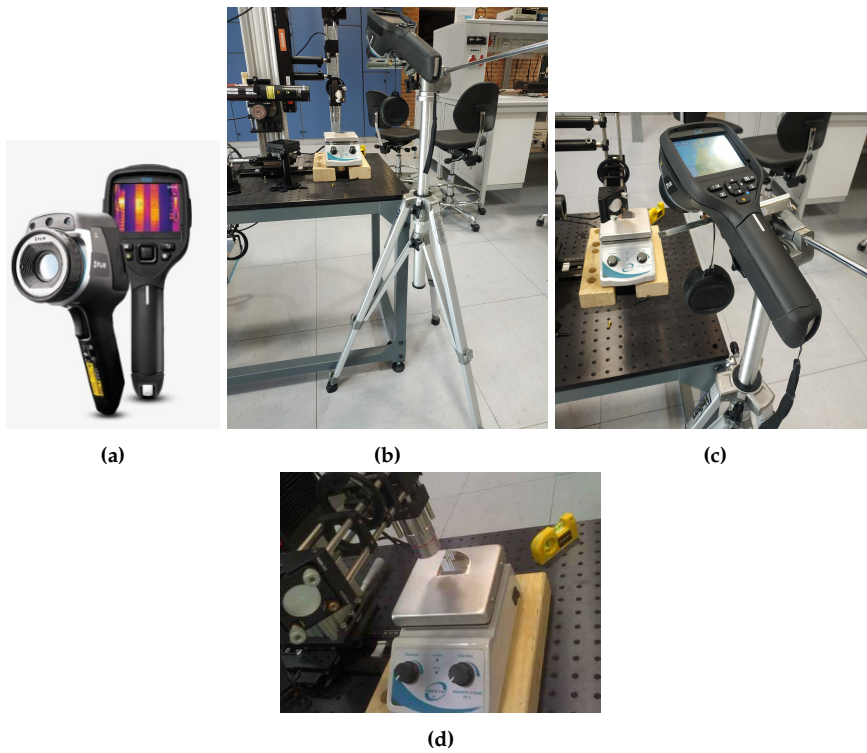
Figure 5.6: (a) IR camera FLIR E40 (b) Camera mounted on the tripoid (c) Close up of the camera mounted ont he tripod (d) Sample on the heater with thermal paste

(a)

(b)

(c)

(d)

(e)

(f)
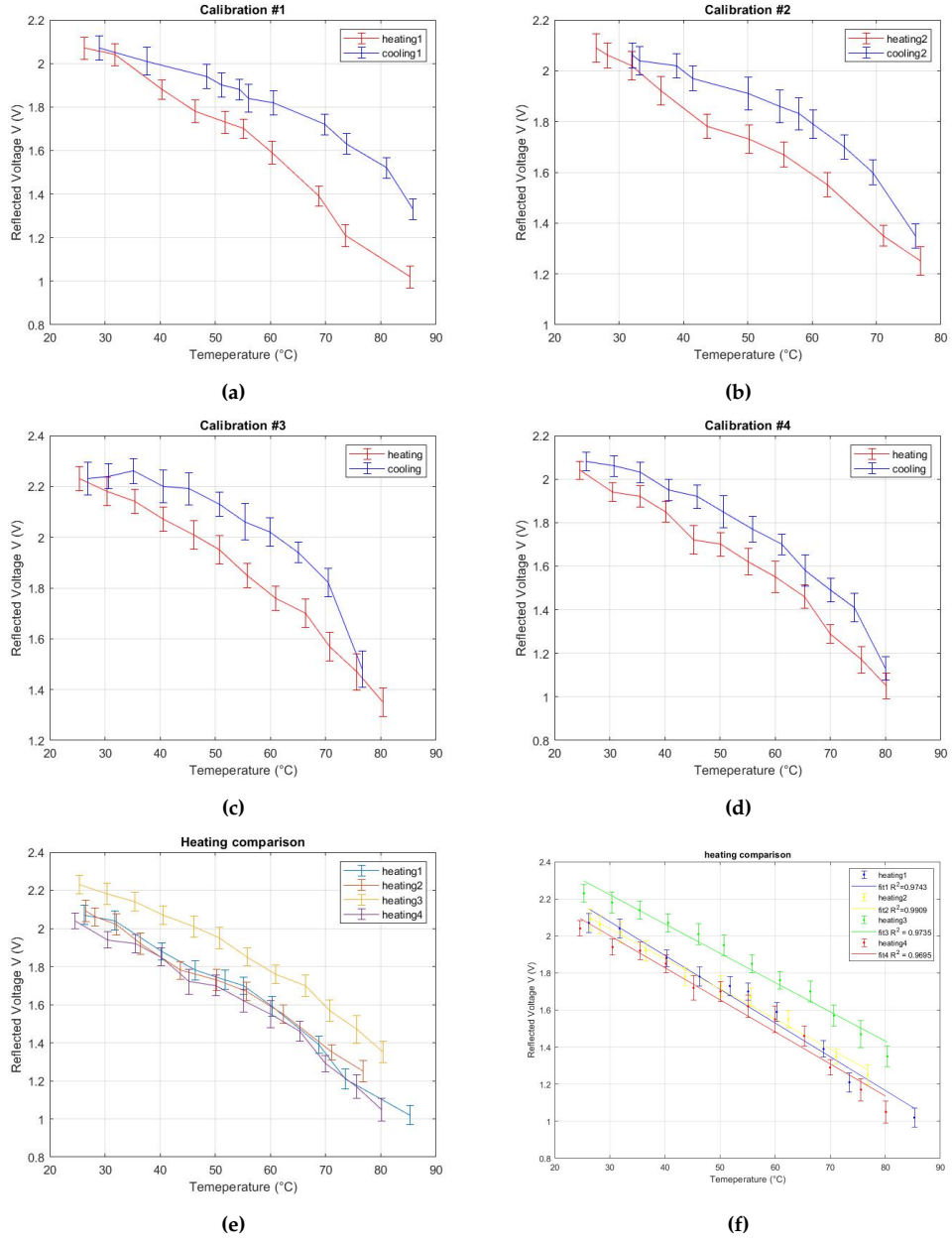
Figure 5.7: Calibration maps elaborated with Matlab
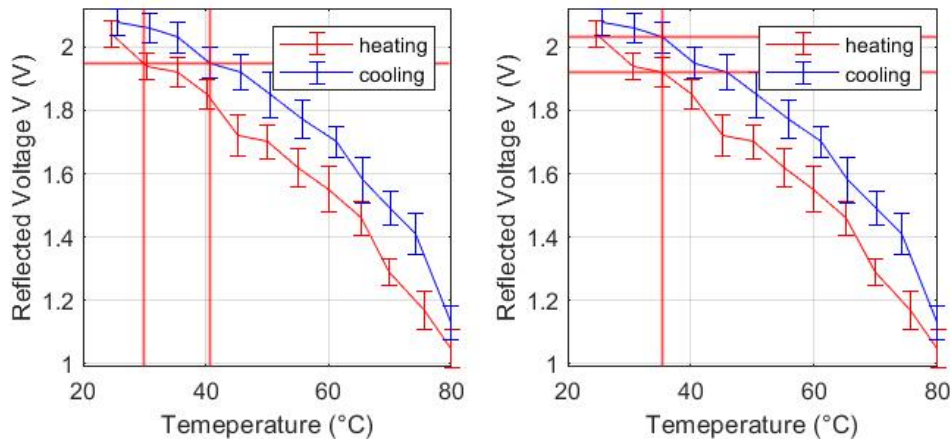
Figure 5.8: (a) Consideration 2 (b) Consideration 3

(a)

(b)

(c)
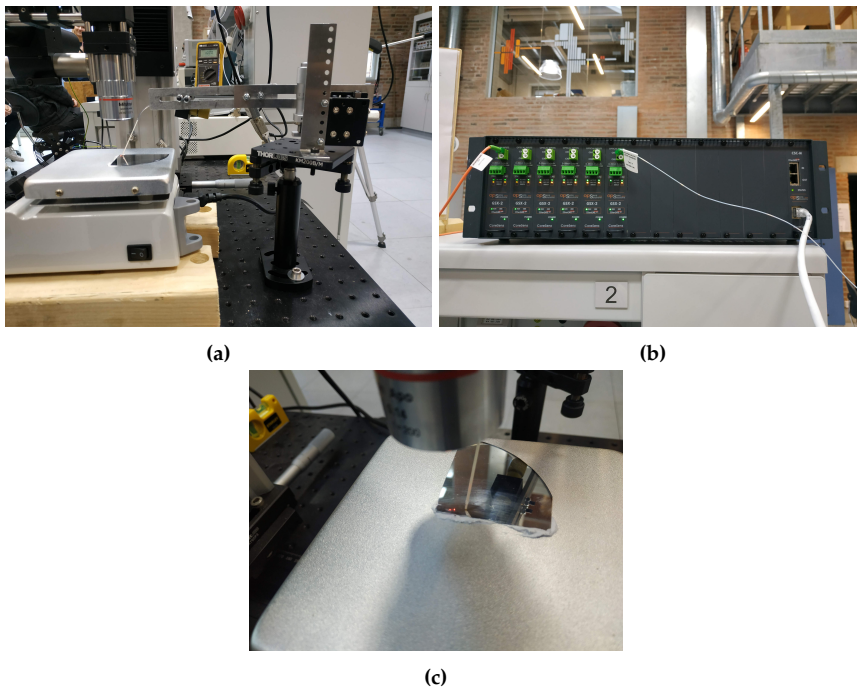
Figure 5.9: Setup for the fiber optics calibration (a) Fiber holder (b) CoreSens signal conditioner (c) Zoom of the position of the fiber on the sample
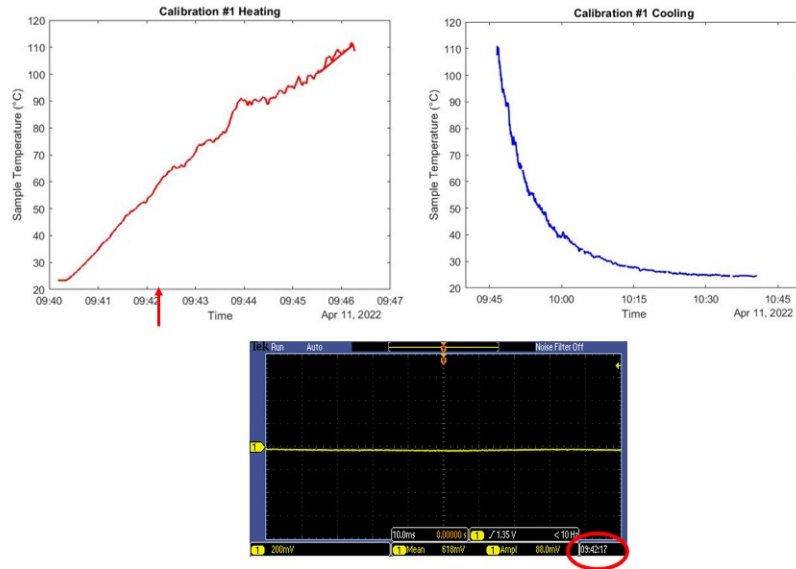
Figure 5.10: Measurement procedure for fiber optics calibration
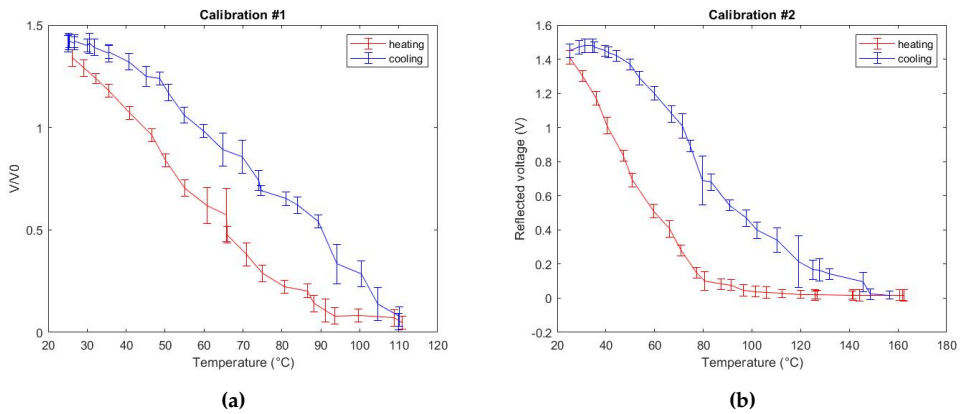
Figure 5.11: (a) Calibration n. 1 map T vs V (b) Calibration n. 2 map T vs V
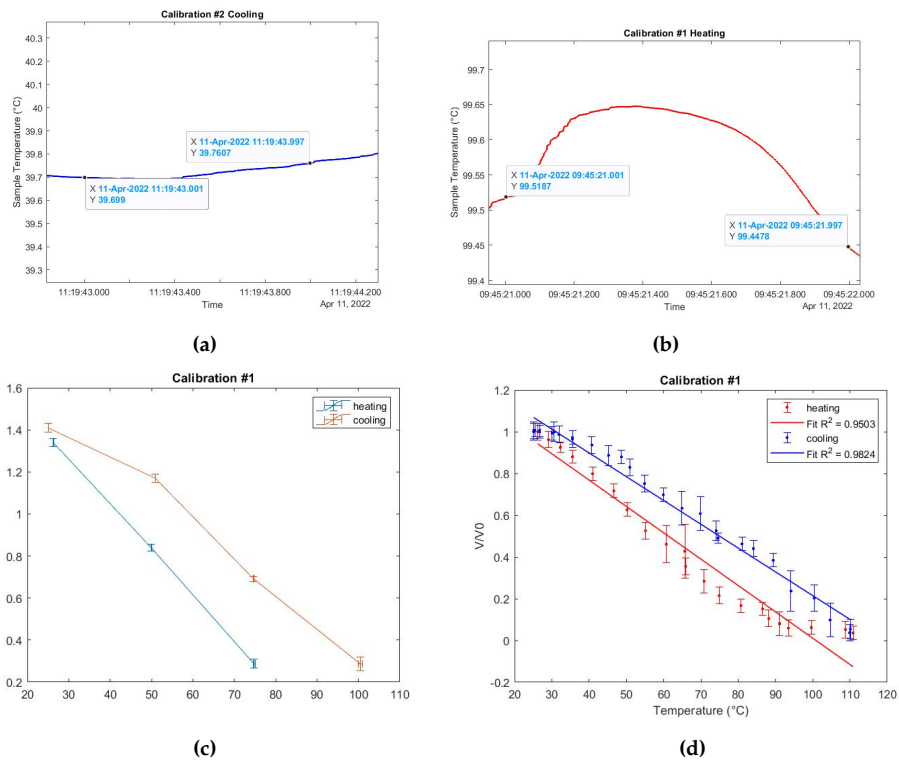
Figure 5.12: (a-b) Zoom of the time vs Temperature graph (c) T vs V map with temperature uncertainty (d) Linear regression fit to the data
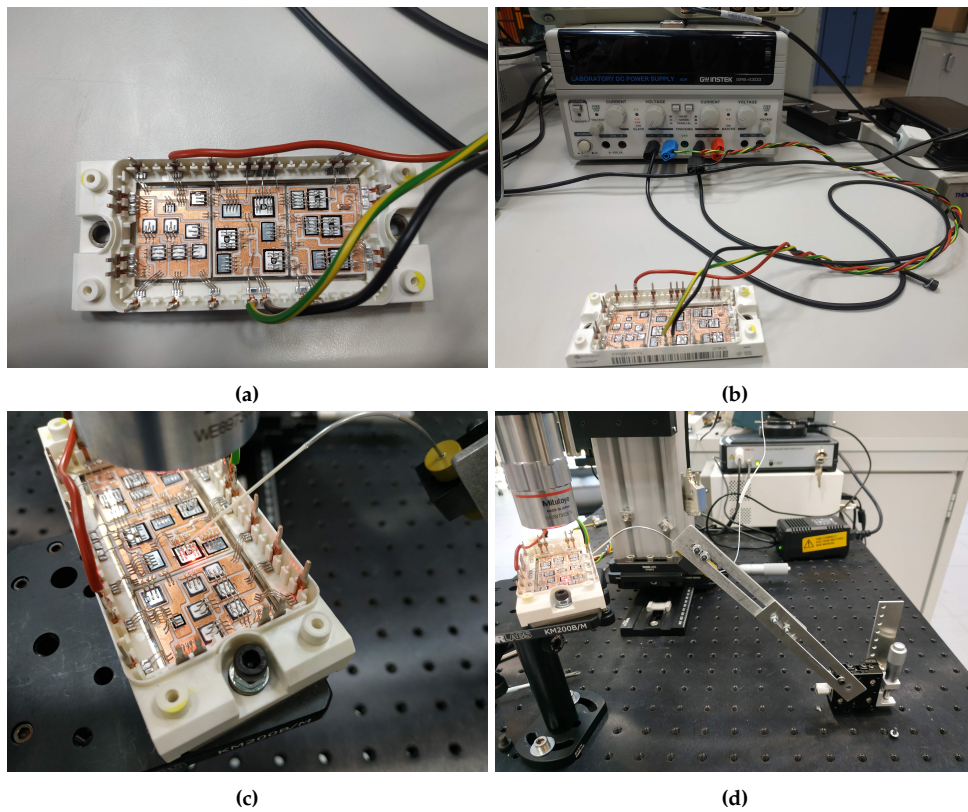
Figure 5.13: (a) IGBT Device used for the measurement (b) DC power supply and device (c) Zoom of the laser spot and the optical fiber on the chip (d) Optical fiber holder
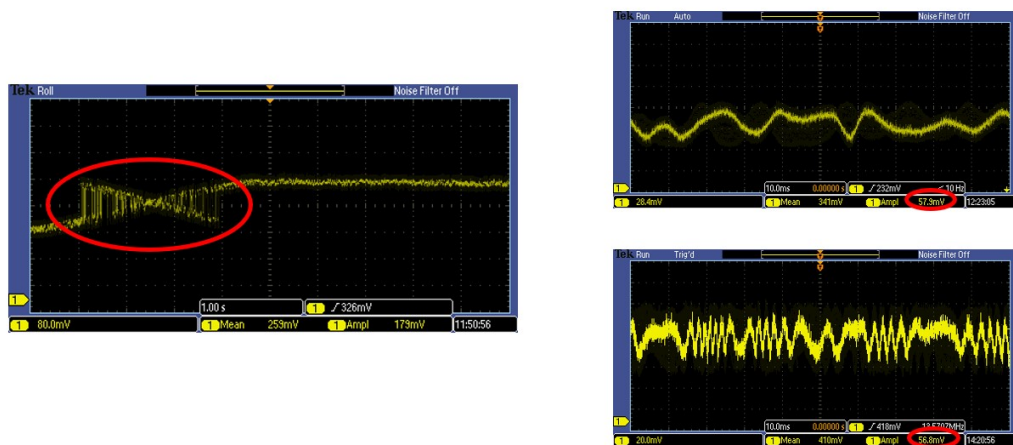
Figure 5.14: Noise of the IGBT measurement. Unwanted optical alignment reflections (left). Greater amplitude flactuations (right).
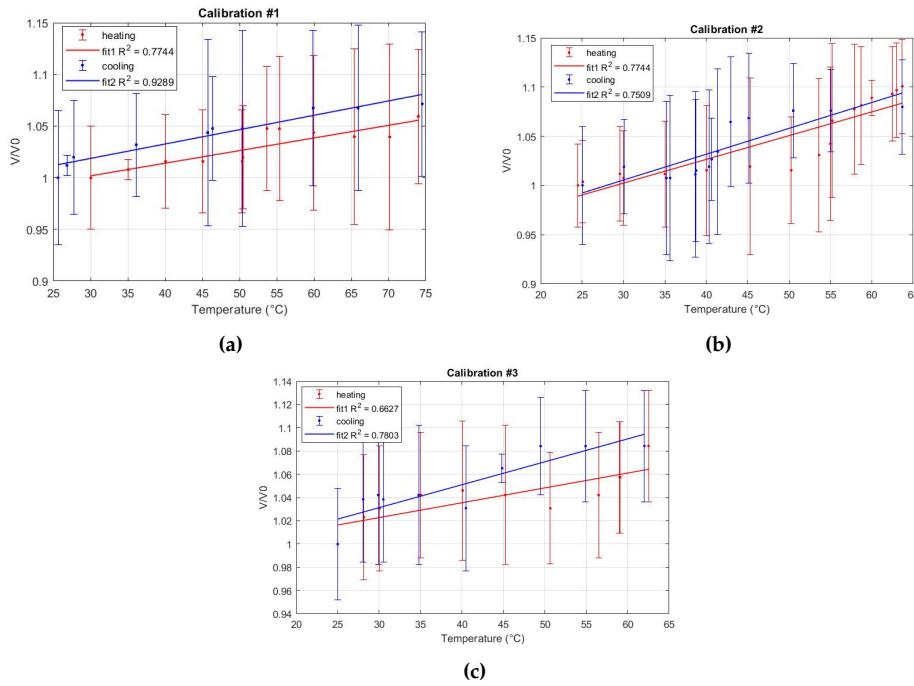
Figure 5.15: Calibration IGBT results
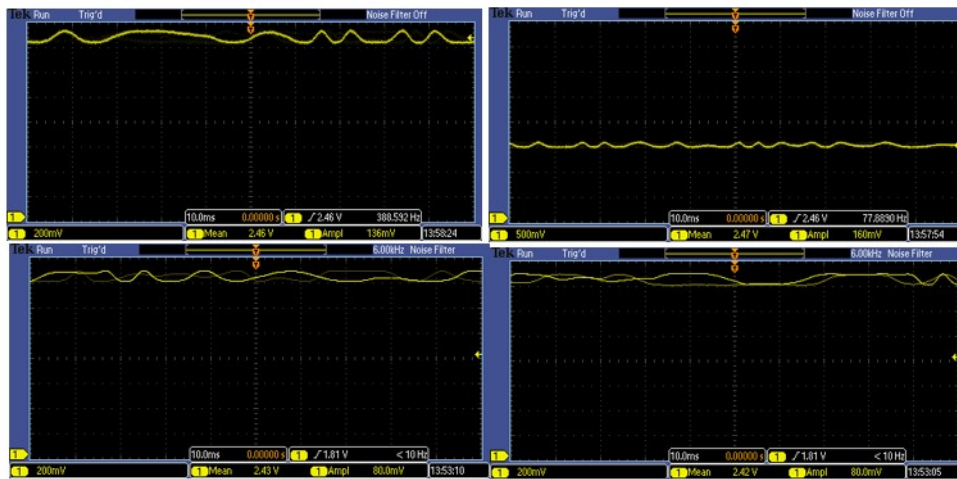
Figure 5.16: Trace with low frequency fluctuations and superimposed thermal noise (upper). Trace with low-pass filter on (lower)
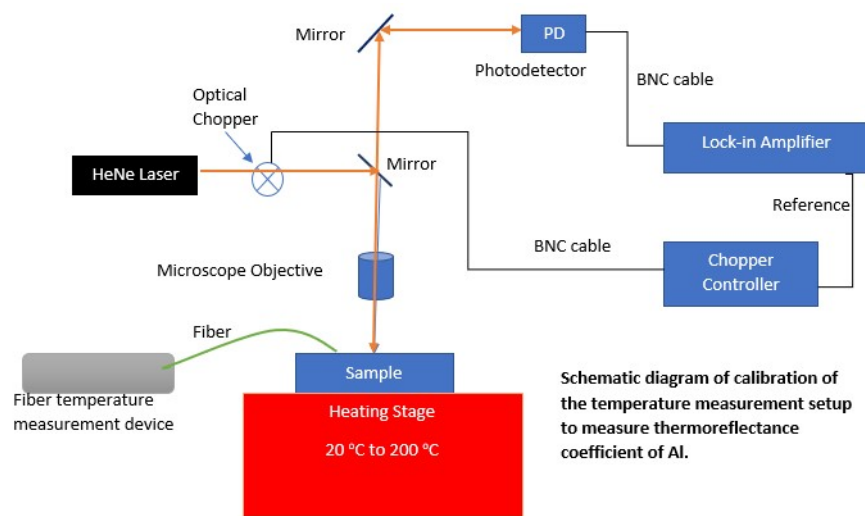
Figure 5.17: Schematic diagram of the calibration setup
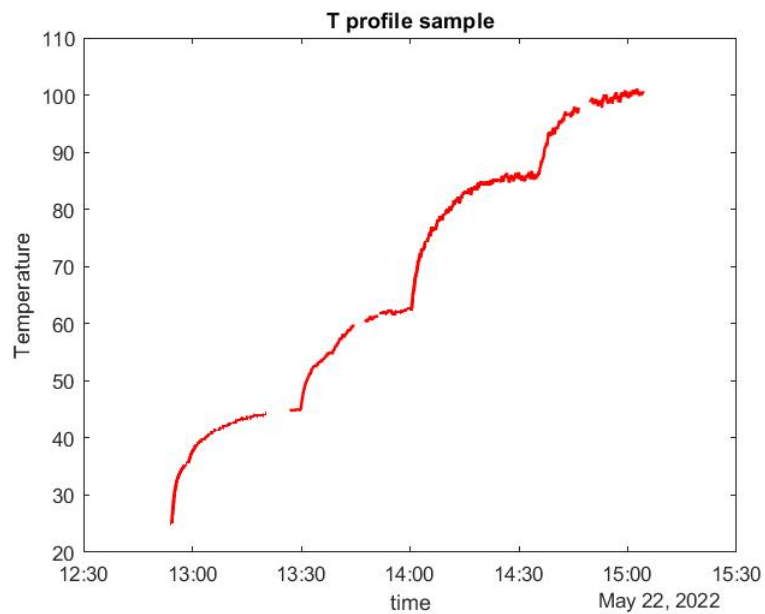
Figure 5.18: T profile from the optical fiber
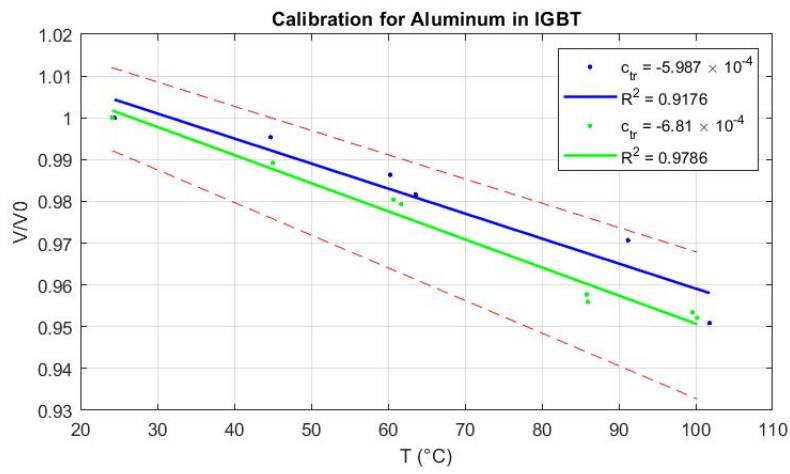
Figure 5.19: Correct calibration of the IGBT metallization. Data plotted with the 95% confidence interval of the second fit (green)
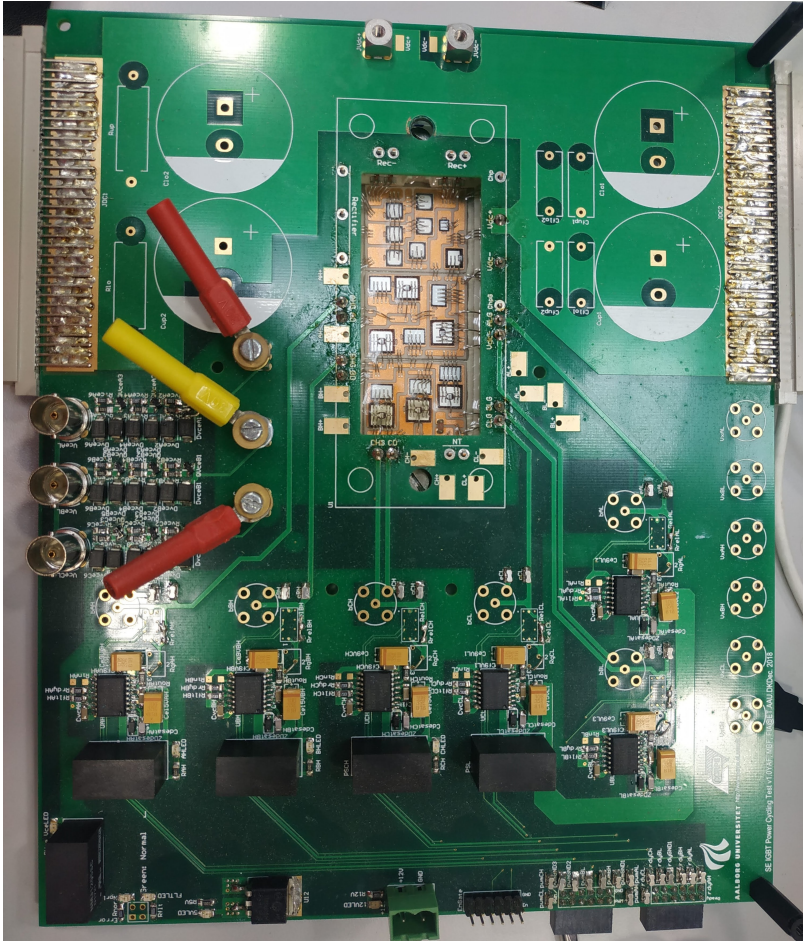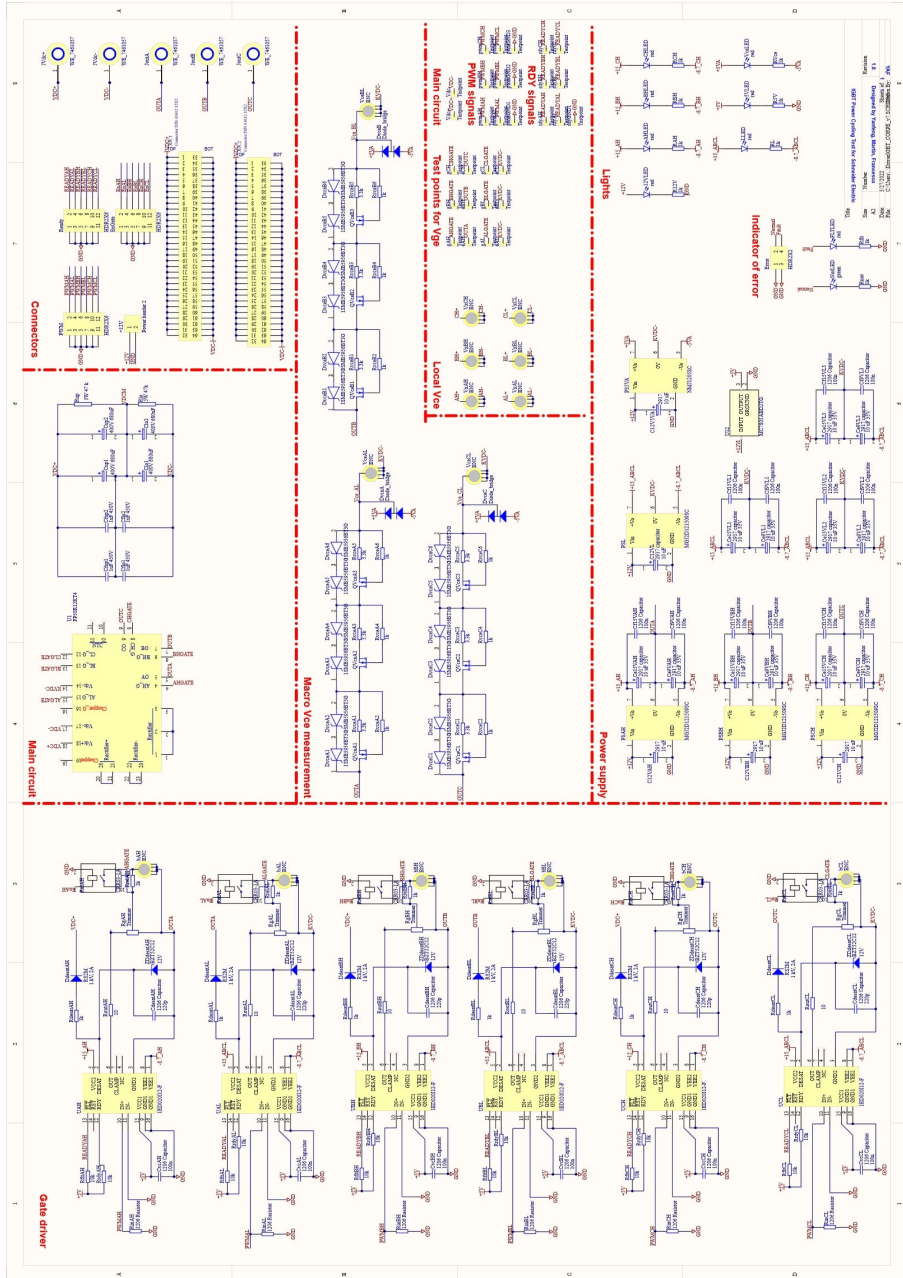
Figure 5.20: PCB board for power cycling test of an IGBT module

Figure 5.21: Schematic of the board for power cycling test
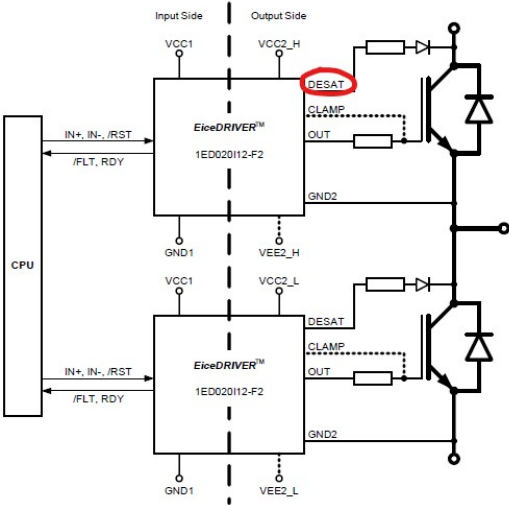
Figure 5.22: Typical application for the gate driver

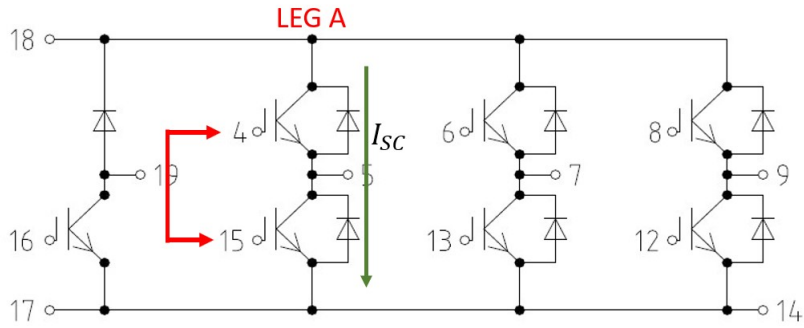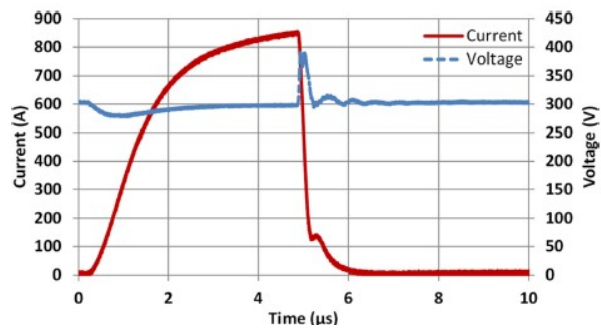**Figure 5.23:** Laboratory setup for conducting short-circuit measurements
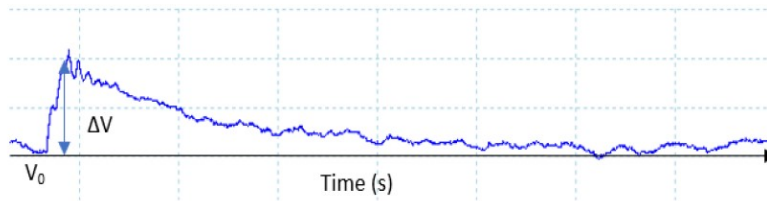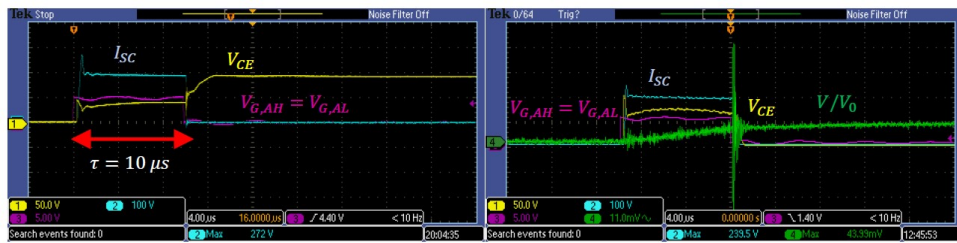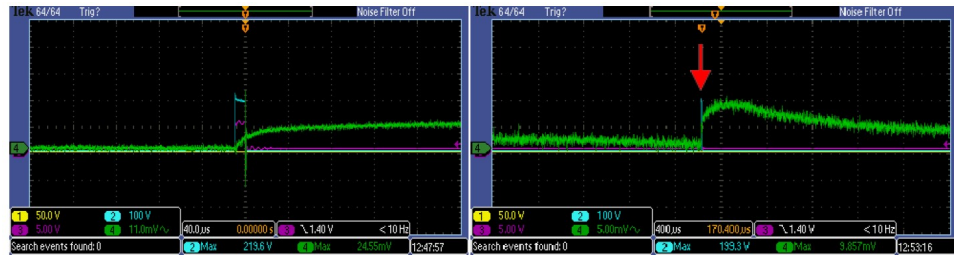
Figure 5.24: IGBT Schematic

(a) Typical short-circuit operation - voltage (blue) current (red) [3]

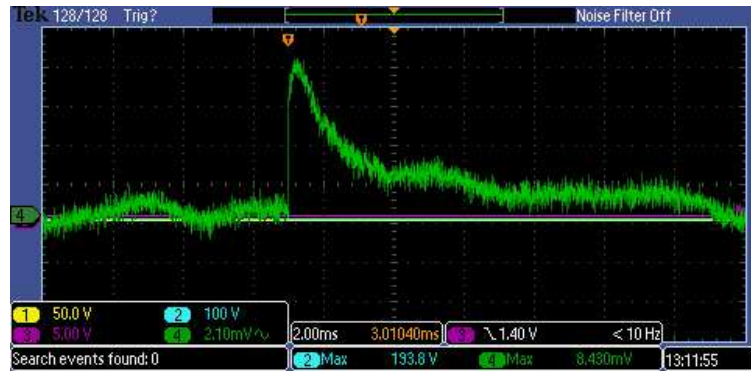**(b)** Typical photothermal signal for short circuit test [29]

(a) Electrical and optical parameters of the IGBT during short circuit - horizontal scale = $40\mu s$
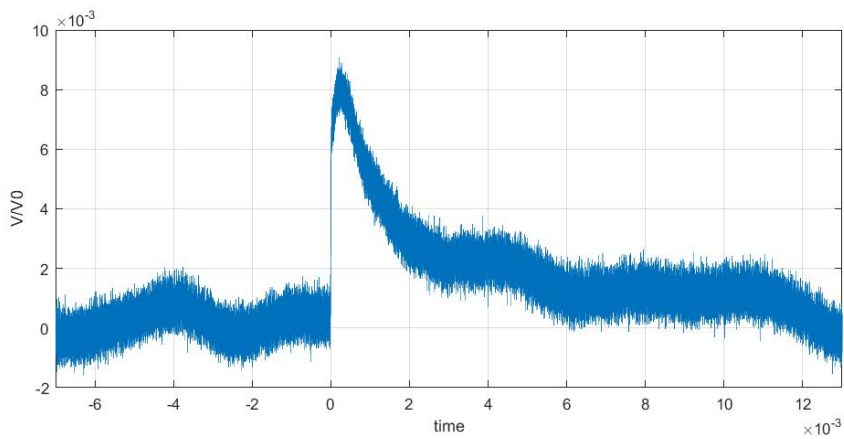

(b) Electrical and optical parameters of the IGBT during short circuit. (Left) horizontal scale = $400\mu s$. (Right) horizontal scale = $4ms$

Figure 5.26: First and second short-circuit measurement

(a) Optical pulse of the IGBT during short circuit - horizontal scale = $20ms$. Supply voltage = $280V$

(b) Data elaboration of the peak

Figure 5.27: Third short-circuit measurement

Chapter 6

Conclusion

In this work it is proven for the first time that laser reflectometry can be applied in the field of power electronics to detect the evolution of the junction temperature of a semiconductor device in short time intervals, in the order of the microseconds, which was not possible with the technology currently available. This can be implemented because the variation in the laser-produced light reflected from the metal surface is measured and correlated to the metal's junction temperature. This is possible thanks to the metal's thermo-optical property that linearly correlates the perturbation of its reflectance to its temperature variation.

In this work encouraging results were presented since it was possible to observe a peak of the measured laser light produced by the temperature excitation of the chip due to the high voltages and currents present across the chip during a short-circuit event.

Estimating directly the temperature can have important consequences on the device design from a reliability point of view.

A very important consideration is that this technique is completely non-invasive and the results reported in this work were obtained without removing the insulating gel deposited on top of the IGBT surface since the optical light is not influenced by the new material. In addition, the silicon gel doesn't modify the alluminum thermoreflectance coefficient, which was determined for a decapsulated module.

The first part of this work was dedicated to the determination of the ther-

moreflectance coefficient for the alluminum metallization on top of the silicon chip.

Initial measurements were conducted with different temperature measurement systems which proved to be not effective since the thermoreflectance variation was buried in noise. An analysis of the origin of the noise highlighted that it was due to both electromagnetic interference and environmental factors. Consequently, a lock-in detection was implemented in conjunction with an optical chopper to alternate the laser light and two peltier cells used as heat generation for a better temperature control. Thus, a possible thermoreflectance coefficient was measurement after implementing the lock-in measurements:

$$\boxed{c_{tr} = -6.81 \times 10^{-4}/^\circ C} \tag{6.1}$$

which is in accordance with typical calibration coefficients for metal layers.

Some open issues include the quantitative estimation of the junction temperature and the possible reduction of the optical noise since the reflectance peak can be buried in noise and not fully visible.

References

[1] URL: https://www.chemeurope.com/en/encyclopedia/Super_low_frequency.html.

[2] Ahmed Abuelnaga, Mehdi Narimani, and Amir Sajjad Bahman. "A review on IGBT module failure modes and lifetime testing". In: *IEEE Access* 9 (2021), pp. 9643–9663. ISSN: 21693536. DOI: 10.1109/ACCESS.2021.3049738.

[3] Amir Sajjad Bahman et al. "Modeling of Short-Circuit-Related Thermal Stress in Aged IGBT Modules". In: *IEEE Transactions on Industry Applications* 53.5 (2017), pp. 4788–4795. ISSN: 00939994. DOI: 10.1109/TIA.2017.2702594.

[4] Manfred A. Biondi and M. P. Garfunkel. "Measurement of the temperature variation of the energy gap in superconducting aluminum". In: *Physical Review Letters* 2.4 (1959), pp. 143–145. ISSN: 00319007. DOI: 10.1103/PhysRevLett.2.143.

[5] Frede Blaabjerg, Marco Liserre, and Ke Ma. "Power electronics converters for wind turbine systems". In: *IEEE Transactions on Industry Applications* 48.2 (2012), pp. 708–719. ISSN: 00939994. DOI: 10.1109/TIA.2011.2181290.

[6] Stuart Bowden and Christiana Honsberg. *Absorption Coefficient*. URL: https://www.pveducation.org/pvcdrom/pn-junctions/absorption-coefficient.

[7] L. Ceccarelli, R. Wu, and F. Iannuzzo. "Evaluating IGBT temperature evolution during short circuit operations using a TSEP-based method".

In: *Microelectronics Reliability* 100-101.July (2019). ISSN: 00262714. DOI: 10.1016/j.microrel.2019.113423.

[8] Uimin Choi. *Studies on Igbt Module To Improve the Reliability of Power Electronic Systems*. 2016, p. 119. ISBN: 9788771125016.

[9] D. L. Decker and V. A. Hodgkin. "Wavelength and temperature dependence of the absolute reflectance of metals at visible and infrared wavelengths." In: *Symposium on Laser Induced Damage In Optical Materials* (1980), pp. 190–200.

[10] H. Ehrenreich, H. R. Philipp, and B. Segall. "Optical properties of aluminum". In: *Physical Review* 132.5 (1963), pp. 1918–1928. ISSN: 0031899X. DOI: 10.1103/PhysRev.132.1918.

[11] T. Favaloro, J. H. Bahk, and A. Shakouri. "Characterization of the temperature dependence of the thermoreflectance coefficient for conductive thin films". In: *Review of Scientific Instruments* 86.2 (2015). ISSN: 10897623. DOI: 10.1063/1.4907354. URL: http://dx.doi.org/10.1063/1.4907354.

[12] Yifeng Fu et al. "Graphene related materials for thermal management". In: *2D Materials* 7.1 (2020), ab48d9. ISSN: 20531583. DOI: 10.1088/2053-1583/ab48d9. URL: https://doi.org/10.1088/2053-1583/ab48d9.

[13] Haoxue Han et al. "Functionalization mediates heat transport in graphene nanoflakes". In: *Nature Communications* 7 (2016), pp. 1–9. ISSN: 20411723. DOI: 10.1038/ncomms11281.

[14] Walter A. Harrison. "Band structure of aluminum". In: *Physical Review* 118.5 (1960), pp. 1182–1189. ISSN: 0031899X. DOI: 10.1103/PhysRev.118.1182.

[15] Single Igbt and Driver Ic. "EiceDRIVER ™ Industrial Power Control". In: (2012), pp. 1–34.

[16] Lin Jing et al. "Thermal Conductivity Enhancement of Coaxial Carbon@Boron Nitride Nanotube Arrays". In: *ACS Applied Materials and Interfaces* 9.17 (2017), pp. 14555–14560. ISSN: 19448252. DOI: 10.1021/acsami.7b02154.

[17] O. W. Käding, H. Skurk, and K. E. Goodson. "Thermal conduction in metallized silicon-dioxide layers on silicon". In: *Applied Physics Letters* 65.13 (1994), pp. 1629–1631. ISSN: 00036951. DOI: 10.1063/1.112933.

[18] S. O. Kasap. *Optoelectronics and Photonics: Principles and Practices*. Upper Saddle River, New jersey 07458, 2001.

[19] Soeren Baekhoej Kjaer, John K. Pedersen, and Frede Blaabjerg. "A review of single-phase grid-connected inverters for photovoltaic modules". In: *IEEE Transactions on Industry Applications* 41.5 (2005), pp. 1292–1306. ISSN: 00939994. DOI: 10.1109/TIA.2005.853371.

[20] S. Loughin et al. "Critical point analysis of the interband transition strength of electrons". In: *Journal of Physics D: Applied Physics* 29.7 (1996), pp. 1740–1750. ISSN: 00223727. DOI: 10.1088/0022-3727/29/7/009.

[21] O. Matsuda and O. B. Wright. "Reflection and transmission of light in multilayers perturbed by picosecond strain pulse propagation". In: *Journal of the Optical Society of America B* 19.12 (2002), p. 3028. ISSN: 0740-3224. DOI: 10.1364/josab.19.003028.

[22] L. M. Moore and H. N. Post. "Five years of operating experience at a large, utility-scale photovoltaic generation plant". In: *Journal of Progress in Photovoltaics: Research and Applications* 16 (2008), pp. 249–259.

[23] K. Sturm N. W. Ashcroft. *Interband Absorption and the Optical Properties of Polyvalent Metals*. New York, 1971.

[24] Mikhail Polyanskiy. *Refractive index database*. 2008–2022. URL: https://refractiveindex.info/?shelf=main&book=Si&page=Aspnes.

[25] V. Quintard et al. "Laser beam thermography of circuits in the particular case of passivated semiconductors". In: 31 (1996), pp. 291–298.

[26] Reliawind. "Report on wind turbine reliability profiles—field data reliability analysis". In: (2011). URL: https://cordis.europa.eu/project/id/212966/reporting.

[27]   M. K. Samani et al. "Thermal conductivity of titanium aluminum sili-
        con nitride coatings deposited by lateral rotating cathode arc". In: *Thin
        Solid Films* 537 (2013), pp. 108–112. ISSN: 00406090. DOI: `10.1016/j.
        tsf.2013.04.029`. URL: `http://dx.doi.org/10.1016/j.tsf.2013.
        04.029`.

[28]   Tsutomu Satō. "Spectral Emissivity of Silicon". In: *Japanese Journal of
        Applied Physics* 6.3 (1967), pp. 339–347. ISSN: 0021-4922. DOI: `10.1143/
        jjap.6.339`.

[29]   Infotiv Technology and Development Ab. "Temperature measurement
        setup for short circuit test - Guide". In: 1.19 ().

[30]   G. Tessier, S. Holé, and D. Fournier. "Quantitative thermal imaging
        by synchronous thermoreflectance with optimized illumination wave-
        lengths". In: *Applied Physics Letters* 78.16 (2001), pp. 2267–2269. ISSN:
        00036951. DOI: `10.1063/1.1363696`.

[31]   Huai Wang, Marco Liserre, and Frede Blaabjerg. "Toward reliable
        power electronics: Challenges, design tools, and opportunities". In:
        IEEE Industrial Electronics Magazine 7.2 (2013), pp. 17–26. ISSN: 19324529.
        DOI: `10.1109/MIE.2013.2252958`.

[32]   E. Wolfgang. "Examples for failures in power electronics systems". In:
        ECPE Tutorial Reliability Power Electronics Systems, Nuremberg, Germany
        (2007).

[33]   Shaoyong Yang et al. "An industry-based survey of reliability in power
        electronic converters". In: *IEEE Transactions on Industry Applications* 47.3
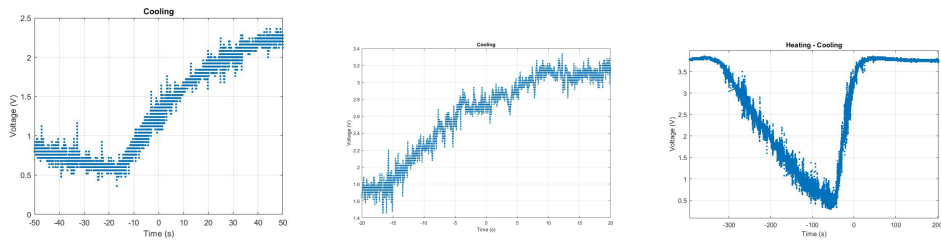   (2011), pp. 1441–1451. ISSN: 00939994. DOI: `10.1109/TIA.2011.2124436`.

Appendix A

Experiment results

A.1 Silicon sample with Aluminum coating
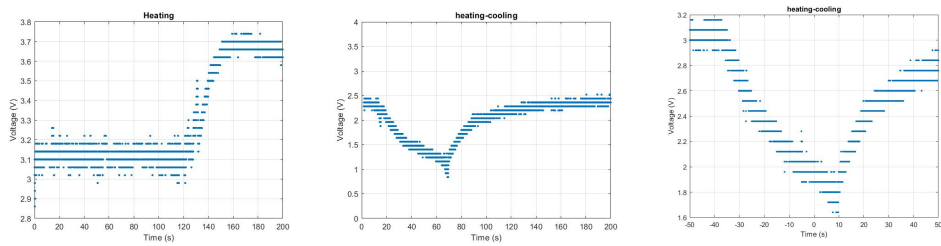
(a) First Measurement: only heating phase

(b) Second Measurement: heating and then cooling

(c) Third Measurement: heating and then cooling

(d) Fourth Measurement: heating and then cooling

(e) Fifth Measurement: only cooling phase

(f) Sixth Measurement: heating and then cooling

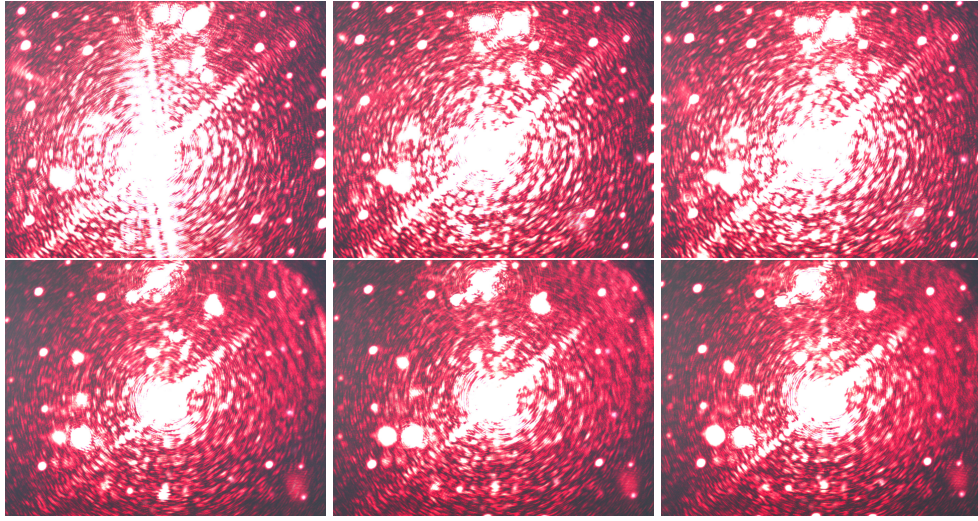**Figure A.1:** Initial measurement of the laser reflectometry

Figure A.2: Laser spot on the sample captured with the CCD during heating

A.2   IGBT - Calibration first experiment

Here are presented the results of the thermoreflectance coefficient for the first calibration attempt for the IGBT.

Calibration phase	$c_{tr}(/^\circ C)$	R^2
Heating 1	1.221×10^{-3}	0.7744
Cooling 1	1.39×10^{-3}	0.9289
Heating 2	2.411×10^{-3}	0.7744
Cooling 2	2.627×10^{-3}	0.7509
Heating 3	1.277×10^{-3}	0.7744
Cooling 3	1.972×10^{-3}	0.7803

Table A.1: Thermoreflectance coefficients - slope of the heating and cooling phase of the three calibration maps

A.3   IGBT - Calibration second experiment

Here is presented the waveforms of the photodetector and the chopper. The two signals are square wave at the same frequency of $100Hz$. They present a

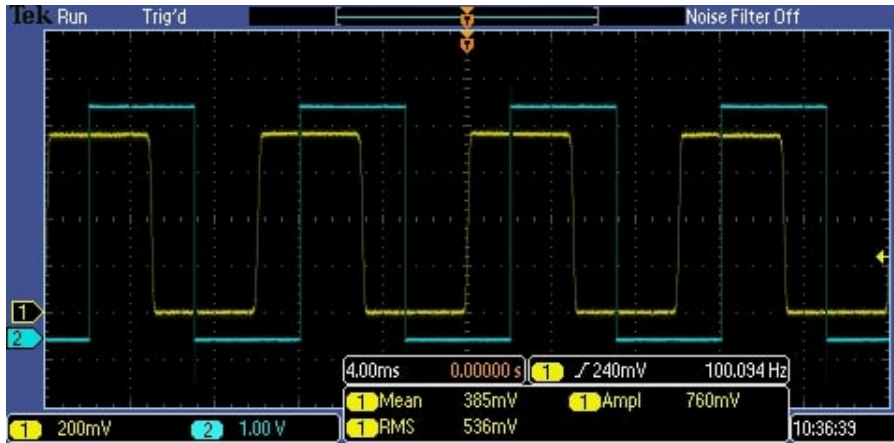phase delay of $\varphi = 72°$, which is present due to the physical distance between the two components.

Figure A.3: Photodetector signal (yellow). Chopper signal (blue)

Appendix B

Equipment details

In fig. B.1 is presented the frequency response of the photodetector. In fig. B.2 is presented the gain curve of the He-Ne laser.
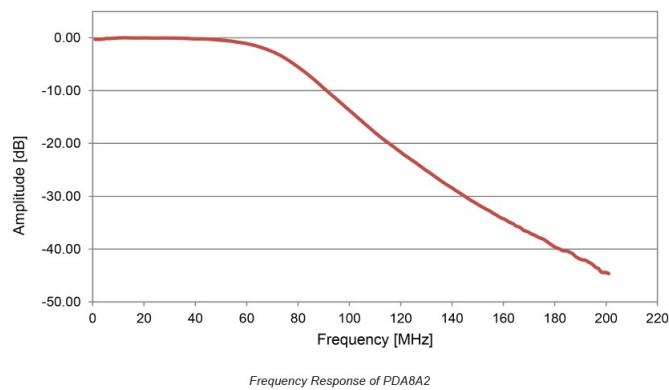

Frequency Response of PDA8A2

Figure B.1: Frequency response of the photodetector

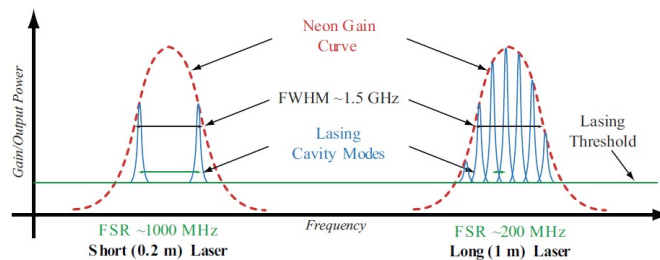In fig. B.3 is presented the transmittivity of the microscope.

Figure B.2: Laser gain curve

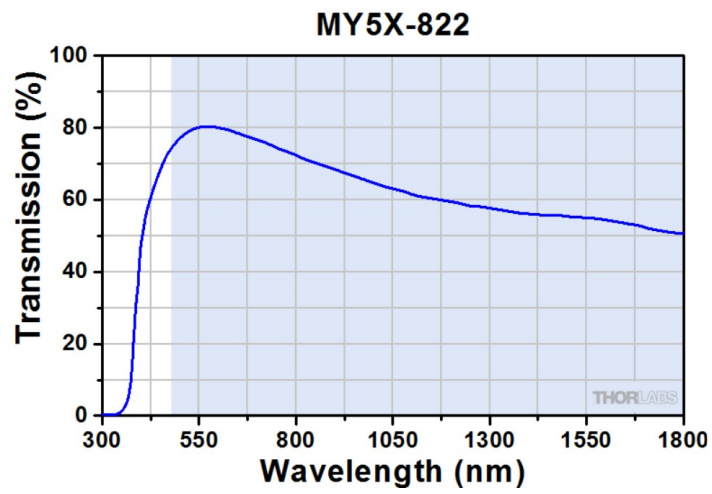In fig. B.4 are presented the devices employed in the second calibration

Figure B.3: Transmittivity of the MO. In blue is indicated the suggested operating wavelengths
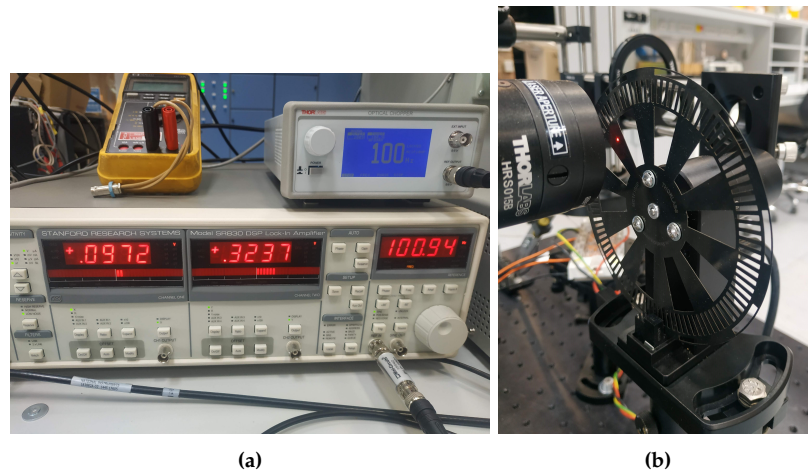
attempt of the IGBT.

(a)   (b)

Figure B.4: (a) Lock-in amplifier (b) Optical chopper head with blade